

Catalyst Induced Hydrino Transition (CIHT) Electrochemical Cell

R. Mills¹, X Yu, Y. Lu, G Chu, J. He, J. Lotoski

BlackLight Power, Inc., 493 Old Trenton Road, Cranbury, NJ 08512, USA

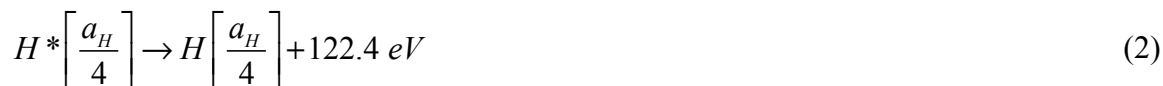
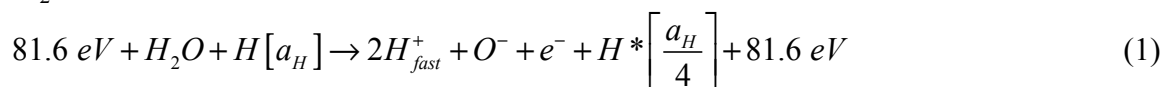
Abstract: Atomic hydrogen is predicted to form fractional Rydberg energy states $H(1/p)$ called "hydrino atoms" wherein $n = \frac{1}{2}, \frac{1}{3}, \frac{1}{4}, \dots, \frac{1}{p}$ ($p \leq 137$ is an integer) replaces the well-known parameter $n = \text{integer}$ in the Rydberg equation for hydrogen excited states. The transition of H to a stable hydrino state $H\left[\frac{a_H}{p = m + 1}\right]$ having a binding energy of $p^2 \cdot 13.6 \text{ eV}$ occurs by a nonradiative resonance energy transfer of $m \cdot 27.2 \text{ eV}$ (m is an integer) to a matched energy acceptor such as nascent H_2O which has a potential energy of 81.6 eV ($m = 3$) to form an intermediate that decays with the emission of continuum bands with short wavelength cutoffs and energies of $m^2 \cdot 13.6 \text{ eV}$. The predicted $H(1/4)$ continuum radiation in the region 10 to 30 nm was observed first at BlackLight Power, Inc. (BLP) and reproduced at the Harvard Center for Astrophysics (CfA) wherein H_2O catalyst was formed by a hydrogen reduction reaction at the anode of a hydrogen pinch plasma. By the same mechanism, the nascent H_2O molecule formed by an oxidation reaction of OH^- at a hydrogen anode is predicted to serve as a catalyst to form $H(1/4)$ with an energy release of 204 eV compared to the 1.48 eV required to produce H from electrolysis of H_2O . CIHT cells, each comprising a Ni anode, NiO cathode, a LiOH-LiBr eutectic mixture as the electrolyte, and MgO matrix exploit hydrino formation as a half-cell reaction to serve as a new electrical energy source. The cells were operated under intermittent H_2O electrolysis to generate H at the anode and then discharged to form hydrinos wherein trace H_2O vapor was supplied as entrained in an inert gas flow in otherwise closed cells. Net electrical production over the electrolysis input was measured using an Arbin BT 2000 ($<0.1\%$ error) and confirmed using a digital oscilloscope; wherein no theoretical conventional energy was possible. Materials characterizations included those that quantified any compositional change of the electrolyte by elemental analysis using ICPMS, XRF, and XRD, and SEM was performed on the anode. The electrical energies were continuously output over long-duration, measured on different systems, configurations, and modes of operation and were typically multiples of the electrical input that in most cases exceed the input by a factor of greater than 10. Calorimetry of solid fuels that exploited the same catalyst and a similar reaction mechanism showed excess thermal energy greater than 10 times the maximum possible from any conventional reaction. The predicted molecular hydrino $\text{H}_2(1/4)$ was identified as a product of CIHT cells and solid fuels by MAS ^1H NMR, ToF-SIMS, ESI-ToFMS, electron-beam excitation emission spectroscopy, Raman spectroscopy, photoluminescence emission spectroscopy, FTIR, and XPS.

Key Words: new energy source, hydrogen catalysis, electrochemical cell

¹ Corresponding author: 609-490-1090 (phone); 609-490-1066 (fax); rmills@blacklightpower.com

I. Introduction

Classical physical laws predict that atomic hydrogen may undergo a catalytic reaction with certain species, including itself, that can accept energy in integer multiples of the potential energy of atomic hydrogen, $m \cdot 27.2 \text{ eV}$, wherein m is an integer. The predicted reaction involves a resonant, nonradiative energy transfer from otherwise stable atomic hydrogen to the catalyst capable of accepting the energy. The product is $H(1/p)$, fractional Rydberg states of atomic hydrogen called “hydrino atoms,” wherein $n = 1/2, 1/3, 1/4, \dots, 1/p$ ($p \leq 137$ is an integer) replaces the well-known parameter $n = \text{integer}$ in the Rydberg equation for hydrogen excited states. Each hydrino state also comprises an electron, a proton, and a photon, but the field contribution from the photon increases the binding rather than decreasing it corresponding to energy desorption rather than absorption. Since the potential energy of atomic hydrogen is 27.2 eV , $m \text{ H}$ atoms serve as a catalyst of $m \cdot 27.2 \text{ eV}$ for another $(m+1)$ th H atom. For example, an H atom can act as a catalyst for another H by accepting 27.2 eV from it via through-space energy transfer such as by magnetic or induced electric dipole-dipole coupling. In addition to atomic H, a molecule that accepts $m \cdot 27.2 \text{ eV}$ from atomic H with a decrease in the magnitude of the potential energy of the molecule by the same energy may also serve as a catalyst. The potential energy of H_2O is 81.6 eV [1]. Then, by the same mechanism, the nascent H_2O molecule (not hydrogen bonded in solid, liquid, or gaseous state) may serve as a catalyst. Based on the 10% energy change in the heat of vaporization in going from ice at 0°C to water at 100°C , the average number of H bonds per water molecule in boiling water is 3.6 [1]; thus, H_2O must be formed chemically as isolated molecules with suitable activation energy in order to serve as a catalyst to form hydrinos. The catalysis reaction ($m=3$) regarding the potential energy of nascent H_2O is



And, the overall reaction is



After the energy transfer to the catalyst (e.g. Eq. (1)), an intermediate $\text{H}^*\left[\frac{a_H}{m+1}\right]$ is formed having the radius of the H atom and a central field of $m+1$ times the central field of a proton. The radius is predicted to decrease as the electron undergoes radial acceleration to a stable state having a radius of $1/(m+1)$ the radius of the uncatalyzed hydrogen atom, with the release of

$m^2 \cdot 13.6 \text{ eV}$ of energy. The extreme-ultraviolet continuum radiation band due to the $H^* \left[\frac{a_H}{m+1} \right]$

intermediate (e.g. Eq. (2)) is predicted to have a short wavelength cutoff and energy $E_{\left(H \rightarrow H \left[\frac{a_H}{p=m+1} \right] \right)}$ given by

$$E_{\left(H \rightarrow H \left[\frac{a_H}{p=m+1} \right] \right)} = m^2 \cdot 13.6 \text{ eV}; \lambda_{\left(H \rightarrow H \left[\frac{a_H}{p=m+1} \right] \right)} = \frac{91.2}{m^2} \text{ nm} \quad (5)$$

and extending to longer wavelengths than the corresponding cutoff. The continuum radiation band at 10.1 nm and going to longer wavelengths for theoretically predicted transitions of H to lower-energy, so called “hydrino” states, was observed only arising from pulsed pinched hydrogen discharges first at BlackLight Power, Inc. (BLP) and reproduced at the Harvard Center for Astrophysics (CfA) [2-4]. Continuum radiation in the 10 to 30 nm region that matched predicted transitions of H to hydrino states, were observed only arising from pulsed pinched hydrogen discharges with metal oxides that are thermodynamically favorable to undergo H reduction to form HOH catalyst; whereas, those that are unfavorable did not show any continuum even though the low-melting point metals tested are very favorable to forming metal ion plasmas with strong short-wavelength continua in more powerful plasma sources. Similarly, in hydrogen-helium microwave plasma, H undergoing catalysis with H ($m=1$) as the catalyst gives rise to a concerted energy exchange of the total energy of 40.8 eV with the excitation of the He ($1s^2$) to He ($1s^1 2p^1$) transition (58.5 nm, 21.21 eV) yielding broad continuum emission with $\lambda \leq 63.3 \text{ nm}$ ($\geq 19.59 \text{ eV}$). In independent replication experiments, broad 63.3 nm emission of this nature and the continuum radiation have been observed in helium-hydrogen microwave plasmas and in hydrogen pinch plasmas, respectively [5].

Extraordinarily fast H formed by the mechanism of Eq. (3) and resonant kinetic energy transfer during the energy decay step of Eq. (2) for HOH catalyst and m H atoms catalyst was also confirmed [6-7]. Plasma models show that the half-life of fast H is less than about 10^{-6} s . Given an H population of $10^{14} \text{ atoms cm}^{-3}$ observed continuously in discharge plasmas wherein each H has an energy of $>10 \text{ eV}$, the order of magnitude of the expected power is $10\text{-}100 \text{ W cm}^{-3}$. But, such high thermal power is not observed. The mechanism of the formation of fast H+ given by Eq. (3) which may form fast excited H is consistent with the trivial power release associated with the fast H population since the hot population from the mechanism of Eq. (3) is a 100% excited-state population. It only comprises a small fraction of the H inventory and is not representative of the thermal distribution of the much more prevalent balance of the H wherein the latter is statistically excited to an emitting state such that the fast and cold H densities match those of the bulk.

The energy released to form hydrinos may ultimately be converted to thermal energy as measured calorimetrically [8] and may be utilized in Rankine-style electrical power plants [9-10]. An alternative, more elegant system is directed to a hydrino fuel cell called a CIHT (Catalyst-Induced-Hydrino-Transition) cell that generates an electromotive force (EMF) from the catalytic reaction of hydrogen to lower energy (hydrino) states providing direct conversion of the energy released from the hydrino reaction into electricity. Each CIHT cell shown schematically in Figure 1 comprises a cathode, an anode, and an electrolyte that also serves as a source of reactants to form hydrinos. Due to oxidation-reduction half cell reactions, a hydrino-producing reaction mixture is constituted with the migration of electrons through an external circuit and ion mass transport through a separate internal path through the electrolyte to complete an electrical circuit. In one type of electrolytically regenerative CIHT cell, atomic hydrogen and oxygen are intermittently formed by electrolysis of H₂O in the cell, and the hydrogen catalyst and subsequent hydrinos are formed by a reaction of the reaction mixture during cell discharge with a net gain of electrical output.

Specifically, an exemplary tested CIHT cell comprised a nickel mat anode, nickel oxide cathode, and the molten eutectic salt electrolyte LiOH-LiBr. The cell ran off of water supplied as vapor to the cell. The cell was operated under intermittent electrolysis and discharge. Hydrogen and oxygen were generated during the electrolysis phase at the negative and positive electrodes, respectively, and served as the sources of H and nascent H₂O catalyst. The catalyst forming reaction and the counter half-cell reaction that occurred during discharge are given by

Anode:



Cathode:



The overall reaction may be

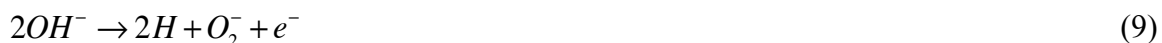


wherein H₂O served as the catalyst. The electrolyte, operating temperature, and H₂O vapor pressure may be controlled such that the standard potential of the electron accepting reaction of Eq. (7) is at essentially 0 V relative to a standard hydrogen electrode to cause a better energy match of the product catalyst with H to facilitate the concerted reaction to hydrino according to Eq. (6).

The power of the hydrino reaction was manifest as an excess current at the operating voltage of the cell set by its conventional chemical composition. A matrix compound comprising oxide ions such as MgO was added to the electrolyte to form a semisolid ion-

conducting paste to further facilitate the hydrino as well as conventional discharge components of the internal ion current. Additionally, the hydrino-reaction-driven excess internal ion current was carried by oxygen containing ions involving oxidation-reduction reactions of the electrolyte and added H₂O that occurred at the electrodes. Based on the Coulomb balance, the internal ion current was significantly manifested and propagated as the spontaneous electrolysis of water. Thus, once initiated, the hydrino reaction may produce electrical power with little to no input electricity. Exemplary ion-carrying, electrolyte-H₂O reactions that also result in H₂O electrolysis are

Anode:



Cathode:



Anode:



Cathode:



Anode:



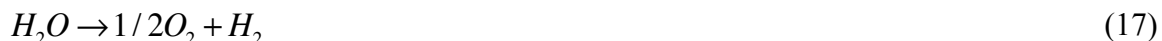
Cathode:



wherein the hydrogen of Eqs. (9), (11), and (13) may react to form hydrinos:



The overall reactions are

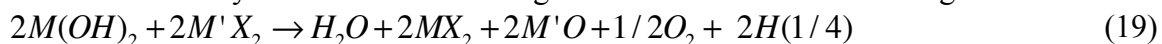


wherein the hydrogen of Eqs. (9), (11), and (13) may additionally react to form H₂O catalyst, and the oxygen of Eqs. (10), (12), and (13) may react and form OH⁻ according to Eqs. (6) and (7) respectively. Other oxygen species such as oxide, peroxide, superoxide, and HOO⁻ and corresponding oxidation-reduction reactions may be involved in the spontaneous electrolysis of H₂O to form at least one of H, catalyst, and hydrinos while carrying the excess current produced by the energy evolved from hydrino formation. CIHT cells were validated by six independent expert scientists or teams to produce as high as 1000 times more electricity out than that required to electrolyze H₂O as the source of hydrogen to form hydrinos. These cells and other scale-up cells served as electrode and electrolyte samples for analytical analysis for the production of the theoretically predicted molecular hydrino product H₂(1/4).

Thermal energy may also be produced from the catalysis of H to H(1/4) wherein nascent H₂O serves as the catalyst, and a chemical reaction is the source of atomic hydrogen and catalyst. The H that reacts to form hydrinos may be nascent H formed by reaction of one or more reactants wherein at least one comprises a source of hydrogen such as the reaction of a hydroxide and an oxide. The reaction may also form H₂O catalyst. The oxide and hydroxide may comprise the same compound. For example, an oxyhydroxide such as FeOOH could dehydrate to provide H₂O catalyst and also provide nascent H for a hydrino reaction during dehydration:



wherein nascent H formed during the reaction reacts to hydrino. Other exemplary reactions are those of a hydroxide and an oxyhydroxide or an oxide such as NaOH + FeOOH or Fe₂O₃ to form an alkali metal oxide such as NaFeO₂ + H₂O wherein nascent H formed during the reaction may form hydrino wherein H₂O serves as the catalyst. Hydroxide ion is both reduced and oxidized in forming H₂O and oxide ion. Oxide ion may react with H₂O to form OH⁻. The same pathway may be obtained with a hydroxide-halide exchange reaction such as the following



wherein exemplary M and M' metals are alkaline earth and transition metals, respectively. An acid-base reaction is another approach to H₂O catalyst. Thus, the thermal chemical reaction is similar to the electrochemical reaction to form hydrinos. Some of these reactions gave a large thermal burst corresponding to rapid exothermic kinetics developing powers well in excess of 200 W in a 43 cm³ volume reactor.

II. Experimental

CIHT Cell Electrical Energy Balance. An exemplary CIHT cell comprised (i) a 6.5 cm ID X 14 cm IH alumina crucible containing the cell components, (ii) a Ni disk anode, 3.8 cm OD, 11 cm², two pressed layers 4 g, porous Ni C6NC (Sumitomo Electric) submersed in electrolyte; alternatively, a Mo or H242 alloy (Haynes) foil anode, 2.5 X 2.5 cm, 6.25cm², 3.5 g and 1.5 g, respectively, (iii) a NiO square cathode, 3.8 cm X 3.8 cm, pre-oxidized porous Ni C6NC (Sumitomo Electric oxidized in air at 350°C for 3 h then 750°C for 4 h) placed on top of electrolyte, and (iv) a molten eutectic salt electrolyte comprising LiOH (15 g)-LiBr (75 g) and MgO matrix (30 g). The electrode spacing was 0.5 cm maintained by the matrix paste. The alumina crucible containing the cell components was placed into a vacuum-tight stainless steel (SS) vessel, 7 cm ID X 25 cm IH, which was sealed with a vacuum tight 10-bolt Conflat flange with a metal gasket. The SS cell was placed in a resistive heater that maintained the temperature of the electrolyte at 450 ± 2 °C. The cell was operated under an argon atmosphere with water vapor at room temperature saturation by flowing 2-10 standard cm³ per minute (sccm) argon (GTS Welco, >99.998 pure) through a water bubbler into the cell through a gas inlet and out of

the cell through a gas outlet that had a water seal from atmospheric air achieved by immersing the outlet gas line under water. The inlet and outlet gas were confirmed to comprise only argon with trace H_2O by on-line mass spectroscopy. Argon was used to purge the initial air atmosphere, and in some cases, the cell was evacuated before flowing argon. In another methodology, a H_2O vapor generator supplied the trace H_2O vapor. The water vapor generator comprised a closed round bottom flask containing degassed water that was heated by a heating mantle such that the water vapor was transported through a thermally insulated line to the top of the SS vessel. Argon was flowed through the vacuum-tight SS vessel containing the CIHT cell for 24 hours, then while maintaining the argon atmosphere, the cell outlet line was closed. Thus, with the argon flow closed, the only input to the cell was water vapor at a pressure controlled by the temperature of the round bottom flask of about 45°C .

Stainless steel leads from the anode and cathode were attached to electrical feed throughs in the flange, and the external electrical connectors were attached to the leads of an Arbin BT2000 fuel cell and battery testing system calibrated within 6 months of usage at Arbin Instruments (College Station TX). The cell was run under intermittent electrolysis conditions. Typically, the programmed waveform comprised the steps of (i) charge at 5 mA constant current until the cell voltage reaches 0.8 V and (ii) discharge at 5 mA constant current until the first of either the cell voltage reaches 0.6 V or 4s duration. For some Mo anodes, the charge voltage limit was typically 1.0 V. The single cells were scaled by using larger surface area electrodes and stacking individual cells with a bipolar plate connecting the anode to cathode, then electrolyte of a repeating unit. The electrical performance of cells comprising a stack of n -cells was similar to that of the corresponding single cell except that the cell charge voltage was set at n -times that of the single cell, and the current was scaled proportionally to the anode surface area. The Arbin BT2000 voltage, current, and power waveforms and energy were confirmed with a digital oscilloscope. Compositional and elemental analyses of the electrolyte were performed by inductively coupled plasma mass spectroscopy (ICPMS), X-ray fluorescence (XRF), and X-ray diffraction (XRD). The anode structure was confirmed intact using scanning electron microscopy (SEM) with elemental analysis by energy-dispersive X-ray spectroscopy (SEM-EDX).

Digital Oscilloscope Confirmation of the CIHT Cell Electrical Energy Balance. The Arbin measurements were confirmed with a data acquisition system (DAS) comprising a PC with Labview 6033E data acquisition card and Labview VI, SCB100 breakout box, and two differential input channels. One being a voltage channel biased to ground across a $5\text{ M}\Omega$ resistor, and the other being a voltage channel measuring current by an IR drop across a $1\text{ }\Omega$ 1% precision resistor also biased to ground across a $5\text{ M}\Omega$ resistor. The DAS was tested against a NIST traceable calibrated Fluke 45 and the voltage and current measurement were confirmed to

be accurate to within ~ 1 mV, < 1 mA. The DAS was also tested against a dual square waveform generated by an Agilent 33220A 20 MHz Arbitrary Waveform Generator and compared to a Tektronix TDS 3054B 500 MHz 5 GS/s Oscilloscope. The major test waveform comprised a 2 Hz cycle, 300 ms on pulse, 0.2 V p-p, and the minor test waveform comprised a 166 Hz cycle, 600 μ s on pulse, 40 mV p-p. Sample data was obtained at 10 KS/s on both the DAS and oscilloscope and both the major and minor waveforms were clearly resolved, and $V \cdot t$ areas matched to within 0.6%.

CIHT Control Cells. The LiOH electrolyte provides a cathode half-cell voltage permissive of an energy match to that of the anode half-cell where the nascent H_2O catalyst is formed to permit the energy transfer from H to the catalyst to form hydrinos with electrical energy flow between the concerted half-cell reactions. Although NaOH and KOH-based electrolytes are much more favorable in terms of the kinetics of conventional fuel cell reactions, they provide significantly different half-cell voltages. Moreover, H_2O is required as a source of H_2 to form hydrinos and its pressure is also important to maintain the half-cell voltage relationships necessary for catalysis according to the Nernst equation. Thus, based on the mechanism identical cells to the LiOH-LiBr-MgO cell were run with Na or K replacing Li, or with Li and the absence of H_2O .

Based on the critical role of H_2O in the mechanism and the concomitant additional elimination of contaminant O_2 as a factor in an alternative mechanism for electrical power generation, H_2 and O_2 were provided independently of electrolysis such that the conventional fuel cell reaction could occur and the effect of the presence or absence of H_2O could be determined. Specifically, H_2 was permeated through a hollow Ni tube anode, and O_2 was supplied by flowing dry or wet air to study the difference. The H_2 permeation cell was loaded with chemicals and assembled in a sealed vessel in a glove box having a dry argon atmosphere such that no H_2O could be absorbed by the pre-dried hygroscopic electrolyte. Specifically, a mixture of pre-dried 20.9 g LiOH and 99.4 g LiBr was placed in an alumina crucible (2.84" OD, ~ 4.0 " height), which was placed in a stainless steel Conflat flange cell (2 7/8" ID, 9" height). The cell anode was a H_2 permeable Ni diaphragm made of two pieces of 1.5" OD and 0.020" thickness Ni foils welded together and joined to a 1/4" (OD) Ni H_2 supply tube, and the cell cathode was a Ni foil (2" W x 3" L, 0.005" thickness) attached to a 1/4" (OD) Ni tube that penetrated the flange. Both the anode and cathode were welded into the flange with stainless steel hollow feedthrough (1/4" OD) tubes. The flange cell was placed in a heater with a temperature-controller that maintained the electrolyte temperature at about 430 $^{\circ}C$. Air/ H_2O was supplied to the cell reaction by flowing dry air from a tank (Praxair) through a H_2O bubbler at room temperature into the cell through a port in the flange, and out through the cathode feedthrough. The H_2 pressure to supply hydrogen to the cell via Ni permeation was maintained

at about 810 Torr. The flow gas was switched to dry air supplied by running dry air from a tank (Praxair) through a SiO₂/Zeolite trap. A 100 ohm resistor was used as load.

Cyclic Voltammetry Determination of the O₂ Reduction Rate. The limiting oxygen reduction current at a nickel cathode in different molten alkaline electrolytes of KOH, NaOH, and LiOH with atmospheric air was determined by cyclic voltammetry using a Metrohm AUTOLAB PGSTAT100. The working electrode was a Ni bar, the counter electrode was a Ni tube, the reference electrode was a Ag wire, and the electrolyte was 3.3 moles of LiOH, NaOH, and KOH, and the operating temperature was 500 °C.

Water-Flow, Batch Calorimetry. The energy balance of the solid fuel reaction mixtures were obtained using cylindrical stainless steel reactors of approximately 43 cm³ volume (1" inside diameter (ID), 5" length, and 0.060" wall thickness having an internal thermocouple well) and a water flow calorimeter comprising a vacuum chamber containing each cell and an external water coolant coil that collected 99+% of the energy released in the cell to achieve an error < ±1%. Both the cells and water-flow calorimeter were described previously [11, 12].

Analytical Samples for the Spectroscopic Identification of Molecular Hydrino. CIHT cells having a molten LiOH-LiBr-MgO electrolyte and a single electrode set or a stack of CIHT cells having bipolar-plate electrodes served as sources of the theoretically predicted molecular hydrino product H₂(1/4). Magic angle spinning ¹H nuclear magnetic resonance spectroscopy (MAS ¹H NMR), electron-beam excitation emission spectroscopy, Raman spectroscopy, time-of-flight secondary ion mass spectroscopy (ToF-SIMS), electrospray ionization time-of-flight mass spectroscopy (ESI-ToFMS), photoluminescence emission spectroscopy, Fourier transform infrared (FTIR) spectroscopy, and X-ray photoelectron spectroscopy (XPS) analysis were performed on reaction products. The molecular hydrino samples comprised CIHT electrolyte, CIHT electrodes, solid fuels products, and inorganic compound getters such as KCl, KOH, and KCl-KOH mixture placed in the sealed container of closed CIHT cells or thermal reactors wherein hydrinos generated during operation were trapped in the matrix of the compound that thereby served as a molecular hydrino getter. Starting materials not exposed to a hydrino source served as controls.

Quantitative X-ray diffraction (XRD). XRD was performed on the starting materials and the reaction products using hermetically sealed sample holders (Bruker Model #A100B37) loaded in a glove box under argon, wax sealed, and analyzed with a Siemens D5000 diffractometer using Cu radiation at 40kV/40mA over the range 10° – 80° with a step size of 0.02° and a counting time of 143 seconds per step. Once the patterns had been obtained, the phases were identified with the aid of the ICDD database and quantified by a Rietveld refinement.

MAS ^1H NMR. ^1H MAS NMR was performed on solid samples using a 270 MHz instrument with a spin speed of 4.5 kHz. Chemical shifts were referenced to external TMS.

Low Resolution UV Spectroscopy of Electron-Beam Excited Interstitial $\text{H}_2(1/4)$. Vibration-rotational emission of $\text{H}_2(1/4)$ trapped in the lattice of getters, electrolytes, and chemical reaction products was investigated via electron bombardment of the crystals. Windowless UV spectroscopy of the emission from the electron-beam excitation was recorded using a McPherson 0.2 meter monochromator (Model 302, Seya-Namioka type) equipped with a 1200 lines/mm holographic grating with a platinum coating and a photomultiplier tube (PMT) detector. The wavelength resolution was about 4 nm (FWHM) with an entrance and exit slit width of 500 μm . The increment was 2 nm and the dwell time was 3 s.

High Resolution UV Spectroscopy of Electron-Beam Excited Interstitial $\text{H}_2(1/4)$. The absence of any molecular structure in the e-beam emission was confirmed using high-resolution UV spectroscopy. The e-beam emission source was connected directly to the entrance of a Jobin Yvon Horiba 1250 M spectrometer. The spectrometer had a 1250 mm focal length with a 2400 g/mm grating and a detector comprising a Symphony model, liquid-nitrogen cooled, back illuminated 2048 \times 512 CCD array with an element size of 13.5 $\mu\text{m} \times 13.5 \mu\text{m}$, 16 bit ADC, and 20 KHz and 1 MHz read outs. The CCD resolution due to the finite-pixel-spectral width was very high, 0.04 Å. Using the 2536.52 Å Hg I line with the entrance slit set to the minimum, the measured resolution was 0.10 Å. The spectrometer resolutions with slit widths of 1000 μm , 500 μm , and 100 μm were 3.0 Å, 1.4 Å, and 0.25 Å, respectively, and the wavelength accuracy was ± 1.0 Å verified with the 2536.52 Å and other Hg I lines.

ToF-SIMS Spectroscopy. The crystalline samples were sprinkled onto the surface of a double-sided adhesive tape and characterized using a PHI TRIFT V nanoTOF ToF-SIMS instrument. The primary ion gun utilized an Au source. In order to remove surface contaminants and expose a fresh surface, the samples were sputter-cleaned for 60 seconds prior to data collection. The aperture setting was 100 μm . Data were collected up to 2000 AMU in positive and negative ion modes using three raster sizes/ion doses for each sample: 100 $\mu\text{m} \times 100 \mu\text{m}$, $5.5 \times 10^{11} \text{ ions/cm}^2$; 50 $\mu\text{m} \times 50 \mu\text{m}$, $2.2 \times 10^{12} \text{ ions/cm}^2$; 25 $\mu\text{m} \times 25 \mu\text{m}$, $8.8 \times 10^{12} \text{ ions/cm}^2$. During acquisition, the ion gun was operated using a bunched (pulse width 4 ns bunched to 1 ns) 30 kV beam. Charge neutralization was active, and the post accelerating voltage was 8000 V.

ESI-ToFMS Spectroscopy. Positive ion ESITOFMS analysis was performed on a Mariner ESI TOF system fitted with a standard electrospray interface. The samples were submitted via a syringe pump at a flow rate of 20 $\mu\text{L/min}$. The solvent was acetonitrile:methanol:water:acetic acid (50:25:24:1). In the selection of the solvent, considered factors were sample solubility, surface tension, speed of evaporation, and positive ion formation.

The ESITOFMS was calibrated before each run using Pierce LTQ ESI Positive Ion Calibration Solution (Thermo scientific) containing Caffeine (20 μ g/mL), MRFA (1 μ g/mL) and Ultramark 1621 (0.001%) in a solution of acetonitrile:methanol:water:acetic acid (50:25:24:1).

Raman Spectroscopy. Raman spectroscopy was performed on solid samples using multiple Raman spectrometers, modes, lasers, gratings, and power and other acquisition parameters. A Horiba Jobin Yvon LabRAM Aramis Raman spectrometer with a 325 nm HeCd laser was operated in microscope mode with a magnification of 40X. Typically, 5 s count time and 5 cycles were run per segment. Additionally, spectra were obtained on bulk samples in glass vials on two Thermo Scientific DXR SmartRaman spectrometers, one having a 532 nm diode laser and another having a 780 nm diode laser. The resolution, depending on the instrument focal length, wavelength range, and grating, was typically 1 - 5 cm^{-1} .

FTIR Spectroscopy. FTIR analysis was performed on solid-sample pellets using the transmittance mode of Nicolet 730 and Nicolet 6700 FTIR spectrometers each with a DTGS detector. The samples were handled under an inert atmosphere. The resolution was 1 cm^{-1} .

XPS Spectra. A series of XPS analyses were made on Ni electrode and crystalline samples using a Scienta 300 XPS Spectrometer. The fixed analyzer transmission mode and the sweep acquisition mode were used. The step energy in the survey scan was 0.5 eV , and the step energy in the high-resolution scan was 0.15 eV . In the survey scan, the time per step was 0.4 seconds, and the number of sweeps was 4. $C\ 1s$ at 284.5 eV was used as the internal standard.

III. Results and Discussion

A. CIHT Cell Electrical Energy Balance. The cell construction details, operating temperature, intermittent electrolysis parameters, and cell charge energy, discharge energy, and electrical gain at timed intervals for representative validation cell [Ni/LiOH-LiBr-MgO/NiO] are given in Table 1. The exemplary charge and discharge waveform recorded by the digital oscilloscope (Figure 2) shows that the input charging time to achieve the set point of 0.8 V was under 100 ms; where after, the cell discharged for 4s at very close to the set voltage of 0.8V. The digital oscilloscope measured energy balance matched that of the Arbin system within a few percent. The excess current over the corresponding input Coulombs shown in Figure 2 was carried by the H_2O and electrolyte ion reactions given in Sec. I. The resulting excess discharge current at the nominal charge voltage resulted in a high electrical energy gain. The electrical power was essentially constant over two months of operation wherein the energy generated during discharge was 5.35 Wh compared to 0.27 Wh of input H_2O electrolysis energy at an overall gain of about 20 times. A plot of the accumulated input and output energies and the gain over the duration of the run are given in Figure 3. No energy was theoretically possible for the closed cell that was supplied H_2O only as indicated by the Ni/ H_2O cell voltage of -0.175 V

shown in Table 2. The controls of Na or K replacing Li consumed energy as shown in Tables 3 and 4. Moreover, H₂O was confirmed as an essential requirement to propagate the reaction to produce excess electrical energy by performing continuous discharge with dry argon flow as shown in Table 5. Similar results were obtained for cells with Mo or H242 alloy (Ni-Mo-Cr alloy) anodes ([Mo or H242 alloy/LiOH-LiBr-MgO/NiO]) wherein the theoretical voltage E_0 (Table 6) and the cell voltage based on the Nernst equation (Eq. (22))) could not explain the high operating voltage of 0.8 to 1.1 V and the large energy gains. For representative cells, the data of the identification of the predicted molecular hydrino product H₂(1/4) with the corresponding energy balance parameters are given in Sec. IIID.

Moreover the cells were shown to scale linearly in voltage with the number of cells of a stack, and the power and energy scaled linearly with electrode surface area wherein the charge and discharge currents per unit area were maintained at a constant value and the charge voltage was typically 0.8 V times the number of cells in the stack. For example, a cell comprising 10 layers of [Ni/LiOH-LiBr-MgO/NiO] each having 850 cm² anode surface area was charged to 8 V at 1.5 A and discharged at 1.5 A for 4 s if $V > 6$ V. The cell stack generated 10 W, and at a representative time point of 5.5 days, the energy generated during discharge was 1200.3 Wh compared to 187.6 Wh of input H₂O electrolysis energy at an overall gain of about 6.4 times.

Alternative sources of the excess electricity that scaled were sought. The cell was closed except for the flow of trace H₂O vapor in semiconductor-grade argon as confirmed by on-line mass spectroscopic analysis of the inlet and outlet gas showing no detectable oxygen above background at sub ppm levels. Furthermore, cells that were argon purged and completely sealed to any mass flow with H₂O supplied by a H₂O vapor generator had similar to better performance. Moreover, even if oxygen was present at near atmospheric pressure (a distinct impossibility) and the cell was analyzed from the perspective of a metal-air battery, the net energy was too high to be accounted for even with 100% conversion of the metal to oxide at 100% electrical efficiency. Specifically, the [Ni/LiOH-LiBr-MgO/NiO] cell shown in Table 1 ran for two months before it was stopped for analysis, and produced 5.35 Wh compared to 0.27 Wh of input H₂O electrolysis energy. Fuel cells are typically less than 50% efficient, but considering 100% efficiency of electrolysis (0 ohmic loss) and 100% fuel cell reaction, the net energy is 5.08 Wh (18.6 kJ). Tests on O₂-Ni metal air batteries with oxygen from atmosphere typically yielded less than 10% efficiency. But, considering 100% electrical production efficiency and using the 4.0501g Ni of the anode at the free energy of 166 kJ/mole Ni (Table 7) for the reaction $\text{Ni} + 1/2\text{O}_2 \rightarrow \text{NiO}$, the maximum electricity possible is 3.13 Wh (11.4 kJ), a more realistic expectation being 0.313 Wh (1.14 kJ). Moreover, the anode was completely intact (Figure 4), and the XRD analysis of the electrolyte following the two-month run of continuous electricity production at an essentially constant voltage, power, and gain showed no detectable NiO (Table 8). The oxygen explanation

of the electrical energy gain is also eliminated based on the observed discharge voltage of 0.8V, the kinetics regarding the current, as well as control results. These factors also eliminated the possibility of thermal decomposition of H₂O, the only mass flow into the cell beyond the immediately eliminated argon. Other exotic reactions of the electrolyte or electrodes were also easily excluded as impossible to make electricity from H₂O as confirmed by the XRD analysis and experience in the fuel cell field such as that with molten alkaline, carbonate, and solid oxide fuel cells having Ni electrodes.

Oxygen is considered in detail. Specifically, the oxygen reduction reaction in molten alkaline electrolytes is experimentally confirmed to be first order in O₂ partial pressure of an O₂-H₂O atmosphere favorable for forming the end-product oxygen ion OH⁻. Limiting current measurements of oxygen reduction in molten NaOH at 623 K using a Ni rotating disc electrode and a porous O₂ gas electrode have identified O₂ as the diffusing species to the gas electrode [13]. Kinetic studies have shown that the reaction mechanism is



wherein Eq. (21) is rate determining. The H₂O partial pressure is a critical condition for the hydrino reaction mechanism as demonstrated in cells having LiOH-LiBr electrolytes and nickel electrodes run under intermittent electrolysis under dry argon flow. Excess electricity is produced in a narrow range of trace amounts of H₂O in about 2 sccm H₂O-saturated Ar flow at 298 K. Furthermore, Ar addition experiments under continuous discharge of a cell having a LiOH-LiBr electrolyte show the dramatic power diminution effect of decreasing O₂ partial pressure when O₂ is displaced by flowing argon gas (Table 5). At constant H₂O pressure, the reaction rate is also first order in O₂ pressure according to Eq. (20) as shown by Hayashi et al. [13] since the oxygen ion from direct reduction of oxygen in LiOH is also O₂²⁻ [14].

Moreover, the oxygen reduction rate in KOH melt is two orders of magnitude higher than that of NaOH due to the much higher diffusion rates in KOH [14-15] (Table 9). This result was confirmed by BLP for KOH compared to NaOH, and was extended to LiOH wherein the oxygen reduction current and the corresponding rate was observed to be about sixty times lower in LiOH than KOH, but comparable to that in NaOH (Table 10). Despite the equal or more favorable limiting kinetics, KOH-KBr and NaOH-NaBr molten electrolytic cells were shown not to produce electricity under identical operating conditions as those of LiOH-LiBr electrolytic cells including the flow of H₂O vapor during intermittent electrolysis and discharge (Tables 3 and 4). Regarding the hydrino mechanism, each electrolyte give rises to a substantially different cathodic half-cell voltage under the operating conditions maintained [14]. LiOH is unique in the production of excess electricity since its oxygen half-cell potential sums with that of the anode

half-cell reaction to provide a sink for electrons from H₂O catalyst of H to hydrinos at a cell voltage to facilitate this reaction and produce excess electrical power. The cathode half-cell voltage depends on the reactant and product concentrations according to the Nernst equation and especially on the H₂O concentration directly and indirectly through the corresponding products. The critical requirement of controlled H₂O vapor pressure was demonstrated by abolition of the production of excess electricity in a LiOH-LiBr electrolytic cell when the flow of trace H₂O vapor was removed from the cell even though H₂O was available to the intermittent electrolysis through the dehydration of LiOH to Li₂O and H₂O. Similarly, the voltage dropped from 0.9 V to 0.1 V with a constant 100 ohm load in switching from wet to dry air in the H₂ permeation anode cell wherein the anodic H₂ and cathodic O₂ concentrations remained unchanged. This null result was also observed in the intermittent LiOH-LiBr electrolysis cell with nickel electrodes and flowing dry air.

Next, consider alternative sources of electrical power other than that from the formation of hydrinos. Specifically, the thermal decomposition of H₂O with the production of electricity from the product gases at the cell electrodes is considered as a possible source of the excess electricity of the CIHT cell. This mechanism was shown experimentally to be nonviable by the absence of excess electricity production in KOH-KBr or NaOH-NaBr electrolytic cells operated identically as the LiOH-LiBr cells with flowing H₂O vapor having the replacement of the electrolyte only. In fact, if thermal H₂O dissociation and subsequent electrical power generation were occurring in any of the molten cells, the rate should be exceptionally high in KOH based on its more favorable diffusivity, as evidenced by its 100 times higher O₂ reduction rate and its adoption in commercial alkaline fuel cells.

Another reason to reject the thermal H₂O splitting hypothesis is that the formation of H₂ and O₂ at an electrode will not give rise to voltage. Gas separation would be necessary such that a net pressure of one gas over the other at each of the two electrodes is maintained in steady state. This is very difficult to achieve, despite decades of development in the field of solar thermal [16-17], and no mechanism for gas separation exists in the CIHT cell. But, assume that separation happens by some unknown mechanism without any recombination (problematic for thermal solar systems) or dilution of the gas concentrations. Then, at a total of atmospheric pressure with the limit of H₂O concentration under the operating conditions, the corresponding equilibrium pressure of product H₂ and O₂ are very low, about 10⁻¹⁰ atm [18]. Using the Nernst equation with $p_{H_2O} = 24$ Torr (0.0315 atm), the corresponding voltage is

$$E = E^0 - \frac{RT}{2F} \ln \frac{p_{H_2O}}{p_{H_2} p_{O_2}^{1/2}} = 1.0554 - 1.0713V = -0.0159V \quad (22)$$

where E^0 at 800 K is 1.0554 V ($\Delta G = -203.661 \text{ kJ / mole}$). The H_2O reaction voltage is negative compared to the observed positive voltage that was typically $\sim 0.8 \text{ V}$, another invalidation of the thermal decomposition mechanism.

A more important consideration in electrochemical reactions is the kinetics. The open-circuit voltage may be high in many cases based on the equilibrium thermodynamics, but often insignificant levels of power can be developed due to low kinetics based on transport limitations or high overpotentials due to corresponding activation energies. For example, reconsider that the oxygen reduction rate is first order in O_2 pressure according to Eq. (20). The measured limiting O_2 reduction current in molten LiOH at atmospheric pressure given in Table 9 and implied in Table 10 is about 1.5 mA/cm^2 . Then, by the rate law, the current that is directly proportional to the O_2 partial pressure of 10^{-10} atm is $1.5 \times 10^{-13} \text{ A/cm}^2$, 10^{-10} times less than that of atmospheric pressure. Even considering ppm H_2 and O_2 and using the corresponding Nernst equation (Eq. (22)) open circuit voltage of 0.4 V, the miniscule power is

$$E = VI = (0.4V)(1.5 \times 10^{-13} \text{ A/cm}^2) = 6 \times 10^{-14} \text{ W/cm}^2 \quad (23)$$

Moreover, the most compelling argument against the thermal decomposition of H_2O is the even slower kinetics of H_2O decomposition as experienced by decades of solar thermal H_2O splitting work. According to Lide [16] and Baykara [17], the mechanism even in the 2000 K to 3000 K range on metal surface M involves the first step:



that has an insurmountable energy barrier at 800 K of 500 kJ/mole. The corresponding time to reach 90% of equilibrium concentrations at 2200 K is 10^{-2} s . Consider the result when accepting this 2200 K time constant given that the actual time is an exponentially increasing function of $1/T$. The molecular concentration C of the product gases is given by the ideal gas law:

$$C = \frac{n}{V} = \frac{P}{RT} = \frac{(1.01 \times 10^5 \text{ N/m}^2)(10^{-10})}{(8.31 \text{ Jmol}^{-1}\text{K}^{-1})(800\text{K})} = 1.5 \times 10^{-9} \text{ mol/m}^3 \quad (25)$$

$$= 1.5 \times 10^{-15} \text{ mol/cm}^3$$

Assuming the thermal dissociation reactor volume to be that within the anode displacement and the reaction time to reach 100% of equilibrium being the 10^{-2} s , the power P is

$$P = \frac{(1.5 \times 10^{-15} \text{ mol/cm}^3)(0.1 \text{ cm})(2 \text{ cm})^2 (203.7 \text{ kJ/mol})}{10^{-2} \text{ s}} = 1.2 \times 10^{-8} \text{ W} \quad (26)$$

The calculated results differ from that observed by over five orders of magnitude. The power is miniscule even without consideration of the requirement of 100% gas separation, the negative Nernst voltage (Eq. (22)), and the oxygen reduction rate dependence on O_2 pressure of Eq. (23). Moreover, based on the rate studies, the time to reach 90% of equilibrium at the CIHT cell

temperature [18] is centuries² meaning that this explanation of the source of electricity is impossible.

Based on the chemicals present, other proposed chemistries involving electrochemical reactions were evaluated for the possibility of giving rise to a positive voltage in the CIHT cell, and all were eliminated as well by thermodynamic calculations and absence of corresponding products in the XRD, XRF, SEM, and ICPMS [18-19].

B. Water-Flow, Batch Calorimetry. The energy recovery was determined by integrating the total output power P_T over time. The power was given by

$$P_T = \dot{m} C_p \Delta T \quad (27)$$

where \dot{m} was the mass flow rate, C_p was the specific heat of water, and ΔT was the absolute change in temperature between the inlet and outlet. The reaction was initiated by applying precision power to external heaters. Specifically, 200 W of power was supplied to the heater. During this heating period, the reagents reached a hydrino reaction threshold temperature wherein the onset of reaction was typically confirmed by a rapid rise in cell temperature. Once the cell temperature reached about 400-500 °C the input power was set to zero. To increase the rate of heat transfer to the coolant, the chamber was re-pressurized with 1000 Torr of helium, and the maximum change in water temperature (outlet minus inlet) was approximately 1.2 °C. The assembly was allowed to fully reach equilibrium over a 24-hour period as confirmed by the observation of full equilibrium in the flow thermistors.

In each test, the energy input and energy output were calculated by integration of the corresponding power. The thermal energy in the coolant flow in each time increment was calculated using Eq. (27) by multiplying volume flow rate of water by the water density at 19 °C (0.998 kg/liter), the specific heat of water (4.181 kJ/kg °C), the corrected temperature difference, and the time interval. Values were summed over the entire experiment to obtain the total energy output. The total energy from the cell E_T must equal the energy input E_{in} and any net energy E_{net} . Thus, the net energy was given by

$$E_{net} = E_T - E_{in} \quad (28)$$

From the energy balance, any excess heat E_{ex} was determined relative to the maximum theoretical E_{mt} by

$$E_{ex} = E_{net} - E_{mt} \quad (29)$$

The calibration test results demonstrated a heat coupling of better than 98% of the resistive input to the output coolant, and zero excess heat controls demonstrated that with the calibration correction applied, the calorimeter was accurate to within less than 1% error. The

² The reason why solar thermal H₂O splitting is not economically viable.

results are given in Table 11 where T_{\max} is the maximum cell temperature, and the energy gain is given by $\frac{E_{\text{net}}}{-E_{\text{in}}}$. All theoretical energies are negative when exothermic. Positive output values

represent more output than input energy. Typical energy balances measured by absolute water-flow calorimetry were 3.5 to more than 69 times energy gain relative to the maximum theoretical based on the most exothermic reactions possible, and power levels in excess of 4.5 Wcm^{-3} were reproducibly achieved. Moreover, the chemistries are enabling of thermal regeneration of the products back to reactants as a competitive fuel cycle for thermal power production with H_2O as the source of hydrogen fuel to form hydrinos replacing traditional fossil fuels.

Excess heats from solid fuels reactions measured using water-flow calorimetry have been independently confirmed by differential scanning calorimetry (DSC) runs at testing laboratories. For example, using their commercial DSC 131 Evo instrument on FeOOH serving as a solid fuel to provide H and H_2O catalyst, Setaram Instrumentation based in France measured three times the maximum theoretical heat of forming H_2O and iron oxides. These products were confirmed by XRD using a Bruker D4 diffractometer.

C. Astrophysical and Other Prior Evidence of Hydrinos and Related Energetics. The discovery of high-energy continuum radiation from hydrogen as it forms a more stable hydrino state (Figure 5) wherein the mechanism is further confirmed by the observation of temporally increasing extraordinarily fast H (Figures 6A and B) has astrophysical implications such as hydrinos being candidates for the identity of dark matter and the corresponding emission being the source of high-energy celestial and stellar continuum radiation [4]. By recent astrophysical measurements and mapping, dark matter comprises 98% of the mass of the universe and is ubiquitous (Figure 7). Furthermore, dark matter is shown to be intragalactic by the reformation of massive gravitation bodies from galaxy collision debris wherein the mechanics of those bodies requires massive amounts of non-visible gravitational matter [20-21], and it is has been shown to be collisional [22]. Thus, dark matter would be anticipated to be ubiquitous on Earth as confirmed by the analysis of compounds found to serve as getters for the collection and analytical identification of hydrinos presented in Sec. IIID. Other prior laboratory observations demonstrating the energetics of the hydrino reaction are the formation of hydrogen plasma by heating, its anomalous afterglow duration [23], and the inversion of H lines [24-25]. The energetics of the reaction may be harnessed as electrical and thermal power as reported in Secs. IIIA and IIIB, respectively.

D. Spectroscopic Identification of Molecular Hydrino. MAS ^1H NMR, ToF-SIMS, ESI-ToFMS, electron-beam excitation emission spectroscopy, Raman spectroscopy,

photoluminescence emission spectroscopy, FTIR, and XPS analysis were performed on samples of reaction products comprising CIHT electrolyte, CIHT electrodes, solid fuels products, and inorganic compound getters such as KCl, KOH, and KCl-KOH mixture placed in the sealed container of closed CIHT cells or thermal reactors. The characteristics of molecular hydrino match those of dark matter, and dark matter ($H_2(1/p)$) is anticipated to be present in certain materials capable of entrapping it. Consistent with expectations, the KCl getter contained same naturally abundant $H_2(1/4)$ that was greatly increased with exposure to a source of $H_2(1/4)$.

MAS NMR of molecular hydrino trapped in a protic matrix represents a means to exploit the unique characteristics of molecular hydrino for its identification via its interaction with the matrix. A unique consideration regarding the NMR spectrum is the possible molecular hydrino quantum states. Similar to H_2 excited states, molecular hydrinos $H_2(1/p)$ have states with $l = 0, 1, 2, \dots, p-1$. Even the $l = 0$ quantum state has a relatively large quadrupole moment, and additionally, the corresponding orbital angular momentum of $l \neq 0$ states gives rise to a magnetic moment [1] that could cause an upfield matrix shift. This effect is especially favored when the matrix comprises an exchangeable H such as a matrix having waters of hydration or an alkaline hydroxide solid matrix wherein a local interaction with $H_2(1/p)$ influences a larger population due to rapid exchange. CIHT cell getters such as those comprising KOH-KCl and KCl + K wherein K reacted with H_2O during the hydrino reaction to form KOH showed a shift of the MAS NMR active component of the matrix (KOH) from +4.4 ppm to about -4 to -5 ppm after exposure to the atmosphere inside of the sealed CIHT cell. KCl + K and other getters in solid fuels reactors also showed the upfield shifted NMR effect. For example, the MAS NMR spectrum of the initial KOH-KCl (1:1) getter, the same KOH-KCl (1:1) getter from the scale-up 5 W stack of 10 CIHT cells comprising [Mo/LiOH-LiBr-MgO/NiO] that output 1029 Wh at 137% gain, and the K + KCl getter from the solid fuel reaction of FeOOH (Figures 8, 9, and 10) showed that the known downfield peak of OH matrix shifted from about +4 ppm to the upfield region of about -4 ppm. Molecular hydrino produced by the CIHT cell and solid fuels shifted the matrix from positive to significantly upfield. The different l quantum numbers possible for the $p = 4$ state can give rise to different upfield matrix shifts consistent with observations of multiple such peaks in the region of -4 ppm. The MAS NMR peak of the KOH matrix upfield shifted by forming a complex with molecular hydrino that can be sharp when the upfield shifted hydroxide ion (OH^-) acts as a free rotor, consistent with prior observations. The direct observation of the extraordinary NMR shift of $H_2(1/4)$ may be possible by e-beam or laser heating of the solid getter matrix to convert it from the para to NMR active ortho form to be recorded before essentially 100% re-conversion. MASNMR is necessary to overcome the lack of molecular

rotation at ambient temperature [1]; otherwise, field inhomogeneities could not be averaged out, and the peak would be unobservably broadened [1].

Additional evidence supports the hydrino-based shift mechanism. The ro-vibrational spectrum of $H_2(1/4)$ was observed by electron-beam excitation emission spectroscopy of samples having the upfield shifted MAS NMR spectral peaks. Furthermore, positive ion ToF-SIMS spectra showed multimer clusters of matrix compounds with di-hydrogen as part of the structure, $M:H_2$ ($M = KOH$ or K_2CO_3). Specifically, the positive ion spectra of prior hydrino reaction products comprising KOH and K_2CO_3 [26-27] or having these compounds as getters in CIHT cells showed $K^+(H_2:KOH)_n$ and $K^+(H_2:K_2CO_3)_n$ consistent with $H_2(1/p)$ as a complex in the structure. A typical result shown in Figures 11A-C is that of the positive ToF-SIMS spectrum of K_2CO_3 -KCl (30:70 wt%) getter from the scale-up 5 W stack of 10 CIHT cells comprising [Mo/LiOH-LiBr-MgO/NiO] that output 1029 Wh at 137% gain having the upfield shifted MAS NMR spectral peaks (Figure 9). In the assignment of peaks having nominal mass $m/e = M + 2$, both the high resolution mass and the isotopic abundance of ^{39}K and ^{41}K as well as ^{35}Cl and ^{37}Cl were considered. Similar $M:H_2$ clusters were observed by ESI-ToFMS as given in Table 12. The energy of the interaction of $H_2(1/p)$ and the matrix compound must be greater than that of thermal energies of about 0.025 eV at room temperature since the ToF-SIMS and ESI-ToFMS clusters were stable, and the entire matrix was shifted in some cases in the MAS NMR. The direct identification of molecular hydrino by its characteristic extraordinarily high ro-vibrational energies was sought using electron-beam excitation emission spectroscopy and Raman spectroscopy. Another distinguishing characteristic is that the selection rules for molecular hydrino are different from those of ordinary molecular hydrogen. H_2 excited state lifetimes are very short, and ro-vibrational transitions having $\Delta J = 0, \pm 1$ occur during rapid electronic transitions in H_2 . But, it is not possible for H_2 to undergo a pure ro-vibrational transition having the selection rule $\Delta J = 0, \pm 1$ since $l = 0$ and $\Delta l = \pm 1$ is required in order to conserve angular momentum during the transition. In contrast, such transitions are allowed for molecular hydrinos. The quantum numbers of the atomic electron are p , l , m_l , and m_s [1]. In the case of a hydrino state, the principal quantum number of excited states is replaced by $n = \frac{1}{p}$. Similarly to H_2 excited states, molecular hydrinos have states with $l = 0, 1, 2, \dots, p-1$ wherein the prolate spheroidal photon fields of $H_2(1/p)$; $p = 1, 2, 3, \dots, 137$ have spherical harmonic angular components of quantum number l relative to the semimajor axis [1]. Transitions between these prolate spheroidal harmonic states are permissive of rotational transitions of $\Delta J = 0, \pm 1$ during a pure vibrational transition without an electronic transition as observed for H_2 excited states. The lifetimes of the angular states are sufficiently long such that $H_2(1/p)$ may uniquely undergo a pure ro-vibrational transition having the selection rule $\Delta J = 0, \pm 1$.

The emitting ro-vibrational molecular hydrino state may be excited by a high-energy electron collision or the by a laser wherein due to the rotational energy of $p^2(J+1)0.01509 \text{ eV}$ [1] excited rotational states cannot be populated as a statistical thermodynamic population at ambient temperatures since the corresponding thermal energy is less than 0.02 eV. Thus, the ro-vibrational state population distribution reflects the excitation probability of the external source. Moreover, due to the thirty-five times higher vibrational energy of $p^2 0.515 \text{ eV}$ over the rotational energy, only the first level, $v=1$, is expected to be excited by the external source. Molecular hydrino states can undergo 1 quantum number changes at ambient temperature, and the J quantum state may changed during e-beam or laser irradiation as the power is thermalized. Thus, the initial state may be any one of $l=0,1,2,3$ independently of the J quantum number. Thus, roational and ro-vibrational transitions are Raman and IR active with the R, Q, P branches being allowed wherein the angular momentum is conserved between the rotational and electronic state changes. Permitted by the change in l quantum number, the de-excitation vibrational transition $v=1 \rightarrow v=0$ with a rotational energy up conversion ($J'-J''=-1$), a down conversion ($J'-J''=+1$), and no change ($J'-J''=0$) gives rise to the P, R, and Q branches, respectively. The Q-branch peak corresponding to the pure vibrational transition $v=1 \rightarrow v=0$; $\Delta J=0$ is predicted to be the most intense with a rapid decrease in intensity for the P and R series of transition peaks of higher order wherein due to the available energy of internal conversion, more peaks of higher intensity are expected for the P branch relative to the R branch. An influence of the matrix is expected to cause a vibrational energy shift from that of a free vibrator, and a matrix rotational energy barrier is anticipated to give rise to about the same energy shift to each of the P and R branch peaks manifest as a nonzero intercept of the linear energy separation of the series of rotational peaks.

Ro-vibrational emission of $H_2(1/4)$ trapped in the crystalline lattice of getters was excited by an incident 6 KeV electron gun with a beam current of 10-20 μA in the pressure range of 5×10^{-6} Torr, and recorded by windowless UV spectroscopy. An example of the resolved ro-vibrational spectrum of $H_2(1/4)$ (so called 260 nm band) in the UV transparent matrix KCl that served as a getter in a 5 W CIHT cell stack shows the peak maximum at 258 nm with representative positions of the peaks at 222.7, 233.9, 245.4, 258.0, 272.2, and 287.6 nm, having an equal spacing of 0.2491 eV. The vibrational energy of diatomic molecules such as $H_2(1/p)$ is given by $\sqrt{\frac{k}{\mu}}$ wherein k is the force constant and μ is the reduced mass that is $\frac{1}{2}$ for $H_2(1/p)$. The hydrino molecule is in a crystalline lattice of infinite mass relative to H, and the crystal field mediates a coupling of this mass to vibrational motion that correspondingly shifts the $H_2(1/4)$ vibrational energy. Consequently, the reduced mass for the vibration of a given H

with the other treated as an infinite mass is increased by a factor of two giving a factor of $\frac{1}{\sqrt{2}}$ shift of the vibrational energy. The local thermal equilibrium between the phonons of the matrix lattice and the ro-vibrationally excited molecule is anticipated to result in a cutoff to the energy of the corresponding series of lines at the matrix-shifted vibrational energy with the rotational energy expected to be that of the corresponding free rotor which is the case with H_2 in silicon matrix [28]. Given that the vibrational and rotational energies of $H_2(1/p)$ are p^2 that of H_2 , $p^2 0.515 \text{ eV}$ and $p^2 0.01509 \text{ eV}$ [1], respectively, the ro-vibrational and rotational energies of $H_2(1/4)$ in a crystalline lattice are predicted to have a cutoff of 5.8 eV and an energy spacing of 0.24 eV, respectively. In general, the plot of the energy versus peak number yields a line given by $y = -0.249 \text{ eV} + 5.8 \text{ eV at } R^2 = 0.999$ or better in very good agreement with the predicted values for $H_2(1/4)$ for the transitions $v=1 \rightarrow v=0$ and Q(0), R(0), R(1), R(2), P(1), P(2), P(3), and P(4) wherein Q(0) is identifiable as the most intense peak of the series. Furthermore, the broadening of ro-vibrational transitions of $H_2(1/4)$ relative to ordinary H_2 in a crystalline lattice is expected since the energies involved are extraordinary, being sixteen times higher, and significantly couple to phonon bands of the lattice resulting in resonance broadening.

Another example is the intense 260 nm band comprising the peaks Q(0), R(0), R(1), R(2), P(1), P(2), P(3), and P(4) observed from the KCl getter from a sealed reactor of the gun powder reaction, KNO_3 with softwood charcoal having the formulation C_7H_4O (Figure 12). The 260 nm, e-beam band has no structure other than the broad peaks at 1.4 Å resolution when observed using a Jobin Yvon Horiba 1250 M spectrometer (Figures 13A-B). Additionally, structure was found to be absent at an enhanced 0.25 Å resolution (Figure 13C) as well as at 1.65 cm^{-1} resolution in the photoluminescence spectra shown in Figures 17, 20, and 21 eliminating the possibility of the series comprising unresolved ro-vibrational bands of a common molecule. Different getter matrices such as KCl versus KOH caused a discernible difference in the shift of the position of the center of the series about the Q(0) peak further eliminating the possibility of assignment of the 260 nm band to a series of common gaseous molecular ro-vibrational bands. Rather, the results support broad rotational emission of $H_2(1/4)$ within the $v=1 \rightarrow v=0$ transition as the source. Specifically, the slope matches the predicted rotational energy spacing of 0.249 eV ($p = 4$). The high energetics of the hydrino reaction (200 times conventional chemistry) is possibly a small contributor to the performance of energetic materials such as gun powder based on the observation of $H_2(1/4)$ product since the gun powder reaction is accepted to be well characterized.

The e-beam excitation emission spectrum from KOH getter sealed in the vacuum chamber containing a 65 mW, eight-layer CIHT stack, each cell comprising [Mo/LiBr-LiOH-MgO/NiO], showed a broad continuum emission feature that matched the outline of the profile

of the 260 nm band assigned to $H_2(1/4)$ ro-vibration with a maximum intensity of 6000 counts at about 260 nm. The band that was not observed in the getter starting material was about ten times more intense than typically observed. Intense peaks corresponding to the 260 nm, e-beam band comprising P(1) - P(6) were resolved by Raman spectroscopy. Moreover, the energies and slight barrier to rotation for the corresponding pure rotational series were also confirmed by Raman spectroscopy.

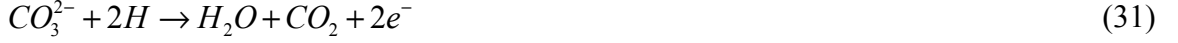
Specifically, $H_2(1/4)$ was also sought using Raman spectroscopy wherein due to the large energy difference between ortho and para, the latter was expected to dominate the population. Given that para is even, the typical selection rule for pure rotational transitions is $\Delta J = \pm 2$ for even integers. However, orbital-rotational angular momentum coupling gives rise to a change in the l quantum number with the conservation of the angular momentum of the photon that excites the rotational level wherein the resonant photon energy is shifted in frequency by the orbital-nuclear hyperfine energy relative to the transition in the absence of the l quantum number change. Moreover, for $l \neq 0$, the nuclei are aligned along the internuclear axis as given in Chp 12 of Ref. [71]. The rotational selection rule for Stokes spectra defined as initial state minus final state is $\Delta J = J' - J'' = -1$, the orbital angular momentum selection rule is $\Delta l = \pm 1$, and the transition becomes allowed by the conservation of angular momentum during the coupling of the rotational and the orbital angular momentum excitations [1]. And, no intensity dependency on nuclear spin is expected. Using a Thermo Scientific DXR SmartRaman with a 532 nm laser in the macro mode, a new sharp Raman peak was observed for the K + KCl getter of the $FeOOH + H_2$ solid fuel at 1950 cm^{-1} (Figure 14) that matching the free space rotational energy of $H_2(1/4)$ (0.2414 eV) for the $J' = 0$ to $J'' = 1$ transition to four significant figures. This result shows that $H_2(1/4)$ is a free rotor which is the case with H_2 in silicon matrix [28].

Since the $H_2(1/4)$ pure rotational transition was also predicted to be FTIR active, the spectrum of K + KCl getter of the $FeOOH + H_2$ solid fuel was recorded with a Nicolet 730 FTIR spectrometer with DTGS detector at resolution of 4 cm^{-1} . The peak corresponding to P(1) was absent in the starting material but was observed as a strong sharp peak at 1947 cm^{-1} in the FTIR spectrum, (Figure 15). Metaborate has a peak in this region, but the ^{10}B peak is absent. Moreover, the Raman spectrum of a metaborate-doped KBr crystal purchased from IC Labs showed no peak in the 1950 cm^{-1} region.

In addition to molten electrolytic cells, the possibility exists to generate H_2O catalyst in aqueous alkaline or carbonate electrolytic cells wherein H is produced on the cathode. Electrode crossover of H formed at the cathode by the reduction of H_2O to $OH^- + H$ can give rise to the reaction of Eq. (6). Alternatively, there are several reactions involving carbonate that can give rise to a H_2O catalyst such as those involving a reversible internal oxidation-reduction reaction such as



as well as half-cell reactions such as



XPS was performed on the Ni cathode of a 0.6 M K_2CO_3 electrolysis cell having Ni electrodes, and a peak was observed at 496.4 eV (Figure 16) that could not be assigned to any known elements. Na being the only possibility was easy to eliminate based on the absence of any other corresponding peaks of this element. The collisional-like Compton ionization to ordinary H states such as H_2^+ is expected with the ionized electron conserving the incident Al X-ray energy as kinetic energy since $H_2(1/4)$ does not absorb or emit radiation and the ionized state to form $H_2^+(1/4)$ is an infinitely excited state. Given that the total energy of $H_2(1/4)$ is 522 eV, the binding of H_2^+ in the Ni lattice with energy comparable to the first ionization energy of H_2 would result in a peak at the observed energy [1]. Depending on the matrix and final H species other shifts in this region are possible. Peaks have been observed on CIHT anodes as well as solid fuel products. The resolution of XPS is insufficient to resolve the splitting due to orbital-nuclear levels associated with different l quantum numbers, but it may be possible using a synchrotron source that would lend further confirmation.

An interrelated confirmatory observation of the identification of hydrino is that the molecular orbital-nuclear coupling energy of $H_2(1/4)$ that is manifest as splitting of the pure rotational Raman transitions is consistent with the spin-nuclear coupling energy predicted and observed for the corresponding atomic hydrino $H(1/4)$. Similar to the case with the 21 cm (1.42 GHz) line of ordinary hydrogen, hydrino atoms were identified by its predicted 642 GHz spin-nuclear hyperfine transition observed by TeraHz absorption spectroscopy of cryogenically cooled H_2 below 35K. Using a long path length (60 m), multi-reflection absorption cell coupled to a Fourier transform interferometer, Wishnow [29] recorded the H_2 spectrum at a spectral resolution of 0.24 cm^{-1} over the wavenumber, temperature, and pressure ranges of 20-320 cm^{-1} , 21-38 K, and 1-3 atmospheres, respectively. A sharp line at 21.4 cm^{-1} was observed at 25.5 K, but is absent at 36 K. The wavenumber of the line is a match to the predicted 21.4 cm^{-1} $H(1/4)$ hyperfine line and could not be assigned to a known species. TeraHz spectroscopy may also serve to identify orbital-nuclear transitions of $H_2(1/4)$.

Another successful cross-confirmatory technique in the search for hydrino spectra involved the use of the by Raman spectrometer wherein the ro-vibration of $H_2(1/4)$ matching the 260 nm e-beam band was observed as second order fluorescence. The first sample comprised the KOH getter from the 65 mW, eight-layer CIHT stack, each cell comprising [Mo/LiBr-LiOH-MgO/NiO], that showed an intense (6000 count) e-beam excitation emission of the 260 nm band

profile. Using the Horiba Jobin Yvon LabRAM Aramis Raman spectrometer with a HeCd 325 nm laser in microscope mode with a magnification of 40X, an intense series of 1000 cm^{-1} equal-energy spaced Raman peaks (Figure 17) were observed at 8340, 9438, 10,467, 11,478, 12,457, 13,433, and 14,402 cm^{-1} with the maximum peak intensity at 12,457 cm^{-1} . The conversion of the Raman spectrum into the fluorescence or photoluminescence spectrum which was then deconvolved (Figure 18) revealed that the Raman spectrum is the superposition of a series of evenly-spaced peaks and a continuum band emission having its maximum intensity at green wavelengths. Green emission was observed from the sample when laser irradiated. Green emission was further observed from the KOH getter sample of Figures 17 and 21 during e-beam excitation to produce the 260 nm band emission assigned to $\text{H}_2(1/4)$ ro-vibration indicating that the series of peaks are a separate spectral feature from the green fluorescence. The fluorescence spectrum in second order calculated from the Raman peak positions of Figure 17 comprises the peaks at 446, 469, 493, 518, 546, 577, and 611 nm. The spacing of 1000 cm^{-1} or 0.1234 eV matches the second order rotational spectrum of $\text{H}_2(1/4)$ very well; thus, the series of peaks matches the second order fluorescence of the 260 nm band first observed by e-beam excitation. In fact, considering the slight contraction at the extremes of the wavelength range due to the matrix shift, halving the wavelength of the calculated fluorescence spectrum and correcting to the transition between matrices results in the e-beam and Raman spectra superimposing (Figure 19), including the peaks intensities. Considering maximum peak intensity at 12,457 cm^{-1} in Figure 17 being Q(0), the assignments are Q(0), R(0), R(1), R(2), R(3), P(1), and P(2) at 12,457, 11,478, 10,467, 9438, 8340, 13,433, and 14,402 cm^{-1} , respectively. The excitation was deemed to be by the high-energy UV and EUV He and Cd emission of the laser wherein the laser optics are transparent to at least 170 nm and the grating (Labram Aramis 2400g/mm 460mm focal length system with 1024 X 26 μm^2 pixels CCD) is dispersive and has its maximum efficiency at the shorter wavelength side of the spectral range, the same range as the 260 nm band. For example, cadmium has a very intense line at 214.4 nm (5.8 eV) that matches the ro-vibrational excitation energy of $\text{H}_2(1/4)$ in KCl matrix based on the e-beam excitation data [30]. The CCD is also most responsive at 500 nm, the region of the second order of the 260 nm band centered at 520 nm. On a repeat scan to higher wavenumbers, additional members of the P-branch of the ro-vibrational series were observed.

The 260 nm band was observed in second order as fluorescence emission of additional reaction products and getters that were shown to comprise $\text{H}_2(1/4)$ by other analytical methods. When $\text{K}_2\text{CO}_3\text{-KCl}$ (1:1) was used as the getter for the cell [laminated-CNi6 1.5"X1.5" + CNi8 1.5"X1.5" + Mo 1"X1" CNi8 + 1.5"X1.5" + Ag 1"X1" + CNi8 1.5"X1.5"+ CNi6 1.5"X1.5")/LiOH-LiBr-MgO/NiO] (50 mA charge and discharge current; 2.65 Wh discharge energy, 200% gain) the 260 nm e-beam band was observed intensely. The Raman spectrum was

recorded to $22,500\text{ cm}^{-1}$, and the corresponding laser-excited second-order fluorescence band having a slight shift due to the different matrix was observed to extend to $17,000\text{ cm}^{-1}$. The series comprised Q(0), R(0), R(1), R(2), R(3), P(1), P(2), P(3), P(4), and P(5) at 12,199, 11,207, 10,191, 9141, 8100, 13,183, 14,168, 15,121, 16,064, and $16,993\text{ cm}^{-1}$, respectively (Figure 20). The photoluminescence band shown in Figures 17 and 20 was also correlated with the upfield shifted NMR peaks. For example, the KOH-KCl (1:1) getter from the scale-up 5 W stack of 10 CIHT cells comprising [Mo/LiOH-LiBr-MgO/NiO] that output 1029 Wh at 137% gain having upfield shifted matrix peaks at -4.06 and -4.41 ppm (Figure 9) showed the series of photoluminescence peaks corresponding to the 260 nm e-beam band (Figure 21). Q(0), R(0), R(1), R(2), R(3), R(4), P(1), P(2), P(3), P(4), P(5), and P(6) were observed at 12,199, 11,207, 10,191, 9141, 8100, 13,183, 14,168, 15,121, 16,064, 16,993, and $17,892\text{ cm}^{-1}$, respectively. This sample also showed intense M:H₂ (M = KOH or K₂CO₃) ToF-SIMS clusters (Figure 11). The equivalent photoluminescence spectrum also observed from getters in solid fuels reactors such as that of KCl + K (to form KOH in situ) getter in the reactor with solid fuel FeOOH + H₂ + Ni screen hydrogen dissociator.

Overall, the Raman results such as the observation of the 0.241 eV (1940 cm^{-1}) Raman peak and the 0.2414 eV-spaced Raman photoluminescence band that matched the 260 nm e-beam spectrum is strong confirmation of molecular hydrino having an internuclear distance that is 1/4 that of H₂. The evidence in the latter case is further substantiated by being in a region having no known first order peaks or possible assignment of matrix peaks at four significant figure agreement with theoretical predictions.

IV. Conclusion

Closed CIHT cells comprising Ni electrodes and a LiOH-LiBr-MgO electrolyte with trace water vapor input only, continuously operated to produce electricity for up to two months until stopped for analysis. The CIHT cells showed multiple times more electrical energy output than that input to generate the hydrogen fuel from H₂O. Each closed cell ran off of H₂O supplied as vapor from which hydrogen and oxygen were generated by intermittent electrolysis and supplied to the electrochemical process of the cell. Due to the electrochemistry occurring in the cell, an electrical current flowed through a load of the electrical testing instrument with an internal ion flow of the ionic-conductive electrolyte completing the electrical circuit. The two currents were permissive of forming hydrinos as the only identifiable source of the multiple times gain in electrical capacity and energy. This conclusion was supported by the absence of any possible known source of electricity based on the corresponding energy balance, and the thermodynamics, kinetics, and analysis of the reaction of the cell components with H₂O or contaminant O₂ as well as the behavior of controls. Calorimetry of solid fuels that exploited the

same nascent H₂O catalyst to form H₂(1/4) with an energy release of 50 MJ/mole H₂ converted, and a similar reaction mechanism showed excess thermal energy greater than 10 times the maximum possible from any conventional reaction, and the predicted molecular hydrino H₂(1/4) was identified as a product of CIHT cells and solid fuels by MAS ¹H NMR, ToF-SIMS, ESI-ToFMS, electron-beam excitation emission spectroscopy, Raman spectroscopy, photoluminescence emission spectroscopy, FTIR, and XPS.

The CIHT cell mechanism of operation involved the concerted formation of H₂O catalyst and hydrinos from atomic H at the anode. The catalyst was formed by the oxidation of the OH⁻ electrolyte with the reaction of H to H₂O that then further catalytically reacted with another H to form hydrino. At 200 times per H that of electrolyzing H₂O to provide the H, the energy released from the formation of hydrinos was dissipated as excess current over that of the anodic OH⁻ oxidation and corresponding H₂O and O₂ reduction at the cathode. Thus, the formation of catalyst and hydrinos with energy release required electron and ion flow corresponding to the production of electricity. A simple summary of the steps of the mechanism is:

1. Assume CIHT is similar to an alkaline fuel cell, except that an electric current is passed through it and an inert atmosphere with trace H₂O vapor surrounds the cathode, anode, and electrolyte.
2. Current is introduced, which produces hydrogen and oxygen from the electrolysis of the supplied trace H₂O. Then, the cell is discharged for a much longer time than it was charged at essentially the same voltage maintained by the energy released from the hydrino reaction.
3. Nascent H₂O is formed at the anode during discharge by oxidation of OH⁻ and reaction with H. Hydrinos are then formed at the anode during cell discharge as a result of the atomic hydrogen reacting with the nascent water that serves as the catalyst to form the hydrinos.
4. When the hydrinos form, energy is given off that causes spontaneous electrochemical reactions to occur at both electrodes that result in a self-propagating electrochemical cycle wherein H₂O is converted to hydrinos, electricity, and oxygen. Specifically, oxidation-reduction reactions of H₂O involving oxygen and oxygen ion intermediates such as hydroxide, oxides, peroxides, and superoxides are involved in the spontaneous electrolysis of water powered by hydrino formation that in turn result in the formation of catalyst and hydrinos. The equivalent of Steps 1 and 2 occur continuously, except that no electricity has been applied during this process. Power is produced with a large net gain in electricity (e.g. 10X) over that to initiate the spontaneous electricity-producing process.

The cell was continuously regenerative and operated at essentially instantaneous steady power output during discharge over long duration as shown by the plot of discharge energy with time (Figure 3). In power applications, a portion of a stack could provide electrolysis power for another and the thermal losses are calculated to be 1% or less such that the system is standalone. The CIHT cell operated under conditions that were similar to those of existing technology such as batteries and fuel cells, but used abundant, nontoxic, commodity chemicals that project a factor of 10 reduction in capital costs relative to conventional electricity sources. The continuous autonomous generation of electricity from H₂O was achieved by a safe, nonpolluting, simple, reliable, sustainable, and inexpensive system operating under standard conditions. The CIHT cell that directly converts H₂O into electricity, molecular hydrino (the dark matter of the universe), and oxygen could be transformational to the energy industry, freeing electrical power, electric motive power, and electric propulsion from any grid or fuels infrastructure.

Acknowledgements

Special thanks to N. Glumac for communications and discussions regarding the molecular hydrino ro-vibrational selection rules and the identification and assessment of alternative mechanisms for the excess electrical energy balances of CIHT cells.

References

1. R. Mills, *The Grand Unified Theory of Classical Physics*; 2011 Edition, in press, posted at <http://www.blacklightpower.com/theory/bookdownload.shtml>.
2. R. L. Mills, R. Booker, Y. Lu, "Soft X-ray continuum radiation from low-energy pinch discharges of hydrogen," submitted.
3. R. L. Mills, Y. Lu, "Time-resolved hydrino continuum transitions with cutoffs at 22.8 nm and 10.1 nm," *Eur. Phys. J. D*, Vol. 64, (2011), pp. 65, DOI: 10.1140/epjd/e2011-20246-5.
4. R. L. Mills, Y. Lu, "Hydrino continuum transitions with cutoffs at 22.8 nm and 10.1 nm," *Int. J. Hydrogen Energy*, Vol. 35, (2010), pp. 8446-8456, doi: 10.1016/j.ijhydene.2010.05.098.
5. A. F. H. van Gessel, Masters Thesis: *EUV spectroscopy of hydrogen plasmas*, April (2009), Eindhoven University of Technology, Department of Applied Physics, Group of Elementary Processes in Gas Discharges, EPG 09-02, pp. 61-70.
6. K. Akhtar, J. Scharer, R. L. Mills, "Substantial Doppler broadening of atomic-hydrogen lines in DC and capacitively coupled RF plasmas," *J. Phys. D, Applied Physics*, Vol. 42, (2009), 42 135207 (2009) doi:10.1088/0022-3727/42/13/135207.
7. R. Mills, K. Akhtar, "Tests of features of field-acceleration models for the extraordinary selective H Balmer α broadening in certain hydrogen mixed plasmas," *Int. J. Hydrogen Energy*, Vol. 34, (2009), pp. 6465-6477.

8. R. L. Mills, G. Zhao, K. Akhtar, Z. Chang, J. He, X. Hu, G. Wu, J. Lotoski, G. Chu, "Thermally reversible hydrino catalyst systems as a new power source," *Int. J. Green Energy*, Vol. 8 (2011), pp. 429–473.
9. R. L. Mills, M. Nansteel, W. Good, G. Zhao, "Design for a BlackLight Power multi-cell thermally coupled reactor based on hydrogen catalyst systems," *International Journal of Energy Research*, Vol. 35, (2011).
10. R. L. Mills, G. Zhao, W. Good, "Continuous thermal power system," *Applied Energy*, Vol. 88, (2011), pp. 789–798, doi: 10.1016/j.apenergy.2010.08.024.
11. R.L. Mills, K. Akhtar, G. Zhao, Z. Chang, J. He, X. Hu, G. Chu, "Commercializable power source using heterogeneous hydrino catalysts," *Int. J. Hydrogen Energy*, Vol. 35, (2010), pp. 395–419, doi: 10.1016/j.ijhydene.2009.10.038.
12. R. L. Mills, G. Zhao, K. Akhtar, Z. Chang, J. He, Y. Lu, W. Good, G. Chu, B. Dhandapani, "Commercializable power source from forming new states of hydrogen," *Int. J. Hydrogen Energy* Vol. 34, (2009), pp. 573–614.
13. H. Hayashi, S. Yoshizawa, "Studies on oxygen reduction in molten NaOH," *Electrochimica Acta*, Vol. 28, No. 2, (1983), pp. 149-153.
14. O.G. Zarubitskii, "The electrochemistry of hydroxide melts," *Russ. Chem. Rev.*, Vol. 49, (1980), pp. 536-548.
15. L. I. Antropov, D. A. Tkalenko, "Reduction of oxygen in alkaline melts", *Elektrokhimiya*, Vol. 6, No. 4, (1970), pp. 595-596.
16. J. Lede, F. Lapique and J. Villiermaux, "Production of hydrogen by direct thermal decomposition of water," *Int. J. Hydrogen Energy*, Vol. 8, (1983), pp. 675-679.
17. S.Z. Baykara, "Experimental solar water thermolysis," *Int. J. Hydrogen Energy*, Vol. 29, (2004), pp. 1459-1469.
18. G. Zhao, "Analysis of water dissociation in the CIHT cell", January (2012), Internal BLP Report (to be posted at www.blacklightpower.com).
19. X. Yu, "Thermodynamic comments", January (2012), Internal BLP Report (to be posted at www.blacklightpower.com).
20. F. Bornaud, P. A. Duc, E. Brinks, M. Boquien, P. Amram, U. Lisenfeld, B. Koribalski, F. Walter, V. Charmandaris, "Missing mass in collisional debris from galaxies," *Science*, Vol. 316, (2007), pp. 1166–1169.
21. B. G. Elmegreen, "Dark matter in galactic collisional debris," *Science*, Vol. 316, (2007), pp. 32-33.
22. M. J. Jee, A. Mahdavi, H. Hoekstra, A. Babul, J. J. Dalcanton, P. Carroll, P. Capak, "A study of the dark core in A520 with the Hubble Space Telescope: The mystery deepens," *Astrophysical J.*, Vol. 747, No. 2, (2012), pp. 96-103.

23. H. Conrads, R. L. Mills, Th. Wrubel, "Emission in the deep vacuum ultraviolet from a plasma formed by incandescently heating hydrogen gas with trace amounts of potassium carbonate," *Plasma Sources Science and Technology*, Vol. 12, (2003), pp. 389-395.
24. R. L. Mills, P. C. Ray, R. M. Mayo, M. Nansteel, B. Dhandapani, J. Phillips, "Spectroscopic study of unique line broadening and inversion in low pressure microwave generated water plasmas," *J. Plasma Physics*, Vol. 71, Part 6, (2005), pp. 877-888.
25. R. L. Mills, P. Ray, R. M. Mayo, "CW HI laser based on a stationary inverted Lyman population formed from incandescently heated hydrogen gas with certain Group I catalysts," *IEEE Transactions on Plasma Science*, Vol. 31, No. 2, (2003), pp. 236-247.
26. R. L. Mills, E. Dayalan, P. Ray, B. Dhandapani, J. He, "Highly stable novel inorganic hydrides from aqueous electrolysis and plasma electrolysis," *Electrochimica Acta*, Vol. 47, No. 24, (2002), pp. 3909-3926.
27. R. L. Mills, B. Dhandapani, M. Nansteel, J. He, T. Shannon, A. Echezuria, "Synthesis and characterization of novel hydride compounds," *Int. J. of Hydrogen Energy*, Vol. 26, No. 4, (2001), pp. 339-367.
28. E. E. Chen, M. Stavola, W. B. Fowler, J. A. Zhou, "Rotation of Molecular Hydrogen in Si: Unambiguous Identification of Ortho-H₂ and Para-D₂," *Phys. Rev. Letts.*, 88(24), (2002), pp. 245503-1 to 245503-4.
29. E.H. Wishnow, *The Far-Infrared Absorption Spectrum of Low Temperature Hydrogen Gas*, Ph.D. Thesis, University of British Columbia, Canada, (1993).
30. <http://physics.nist.gov/PhysRefData/Handbook/Tables/cadmiumtable2.htm>.
31. O. Knacke, O. Kubascheeski, K. Hesselmann, *Thermochemical Properties of Inorganic Substances*, 2nd Ed., Springer-Verlag Berlin, Heidelberg 1991.
32. D. R. Lide, *CRC Handbook of Chemistry and Physics*, 88th Edition, CRC Press, Taylor & Francis, Boca Raton, (2007-8).
33. J. A. Dean, *Lange's Handbook of Chemistry*, Fifteenth Edition, McGraw-Hill Professional, New York, (1999).

Table 1. Validation cell: Flange closed, paste electrolyte [Ni/LiOH-LiBr-MgO/NiO]; Anode—Porous Ni C₆NC (OD 3.8 cm, 11 cm², 4.0501g), submersed into electrolyte; Cathode—Pre-oxidized porous Ni C₆NC (3.8 × 3.8 cm), on top of electrolyte; Electrolyte—15.0 g LiOH + 75.0 g LiBr + 30.0 g MgO; Temperature 450 °C; Flow through Ar (Pre-humidified).

Charge I, T	Discharge I, T	Time	Power density, mW/cm ²	Charge energy, Wh	Discharge energy, Wh	Energy gain, %
5 mA till V=0.8 V	5 mA till V=0.6 V, or 4 s if V>0.6 V in 4 s	1h	0.27	0.0000021	0.0045	214285.7
		18h		0.0008413	0.0734	8724.5
		1d11h		0.0008730	0.1433	16414.6
		4d11h		0.0013	0.4279	32915.3
		5d8h		0.0016	0.4977	31106.6
		6d7h		0.0023	0.5812	25269.5
		7d6h		0.0034	0.6674	19629.4
		8d4h		0.0037	0.7559	20429.7
		11d5h		0.0062	1.0277	16575.8
		12d7h		0.0081	1.1000	13580.2
		13d0h		0.0103	1.1821	11476.6
		13d22h		0.0137	1.2641	9227.0
		14d23h		0.0209	1.3391	6407.1
		17d22h		0.0793	1.5946	2010.8
		18d18h		0.0794	1.6700	2223.1
		19d18h		0.0794	1.7652	2203.7
		20d15h		0.0795	1.8565	2335.2
		21d14h		0.0795	1.9508	2453.8
		24d17h		0.0796	2.2517	2828.8
		25d12h		0.0796	2.3271	2923.5
		26d12h		0.0797	2.4194	3035.6
		27d12h		0.0797	2.5122	3152.1
		28d12h		0.0798	2.6048	3264.2
		31d13h		0.0799	2.8826	3607.8
		32d12h		0.0799	2.9703	3717.5
		33d12h		0.0800	3.0609	3826.1
		34d12h		0.0800	3.1532	3941.5
		35d0h		0.0801	3.1913	3984.1
		38d0h		0.0865	3.4533	3992.3
		39d0h		0.0877	3.5433	4040.3
		40d0h		0.0877	3.6339	4143.6
		41d0h		0.0878	3.7253	4242.9
		41d23h		0.0878	3.8115	4341.1
		44d23h		0.0879	4.0834	4645.5
		45d23h		0.0905	4.1706	4608.4
		46d23h		0.0914	4.2601	4660.9
		47d23h		0.0918	4.3487	4737.1
		48d23h		0.0919	4.4391	4830.4
		51d23h		0.1163	4.6845	4027.9
		52d23h		0.1238	4.7654	3849.3
		53d23h		0.1288	4.8496	3765.2
		54d23h		0.1308	4.9374	3774.8
		55d23h		0.1343	5.0240	3740.9
		58d23h		0.1770	5.2516	2967.0
		59d23h		0.2201	5.2998	2407.9
		61d1h		0.2688	5.3491	1990.0

Table 2. Thermodynamic parameters of the reaction of nickel metal with H₂O at 700 K [30].

Reaction	Ni + H ₂ O to NiO + H ₂			
	Ni	H ₂ O	NiO	H ₂
Stoichiometry	1	1	1	1
HoF@700 K (kJ/mol)	12.351	-227.283	-217.867	11.723
S@700 K (J/molK)	55.603	219.368	83.868	155.545
H	12.351	-227.283	-217.867	11.723
G	-26.571	-380.841	-276.575	-97.159
ΔH _{rxn} (kJ/mol)=	8.788			
ΔG _{rxn} (kJ/mol)=	33.679			
T(K)=	700			
n=	2			
E°(700 K)=	-0.175	Volts		

Table 3. Control Validation cell: Flange closed, paste electrolyte [Ni/NaOH-NaBr-MgO/NiO]; Anode—Porous Ni C₆NC (14 cm², 2.96 g), submersed into electrolyte; Cathode—Pre-oxidized porous Ni C₆NC (3.8 × 3.8 cm), on top of electrolyte; Electrolyte—36 g NaOH + 30 g NaBr + 29 g MgO; Temperature 450 °C; Flow through Ar (Pre-humidified)

Charge I, T	Discharge I, T	Time	Power density, mW/cm ²	Charge energy, Wh	Discharge energy, Wh	Energy gain, %
5 mA till V=0.8 V	5 mA till V=0.6 V, or 4 s if V>0.6 V in 4 s	24 h 38 h	0.32	0.0296 0.0625 ^a	0.0148 0.0148	50.0 27.3

^a Cell continually charged at 0.359 V and could not reach 0.8 V.

Table 4. Control Validation cell: Flange closed, paste electrolyte [Ni/KOH-KBr-MgO/NiO]; Anode—Porous Ni C₆NC (14 cm², 2.92 g), submersed into electrolyte; Cathode—Pre-oxidized porous Ni C₆NC (3.8 × 3.8 cm), on top of electrolyte; Electrolyte—31.4 g KOH + 28.6 g KBr + 22 g MgO; Temperature 450 °C; Flow through Ar (Pre-humidified).

Charge I, T	Discharge I, T	Time	Power density, mW/cm ²	Charge energy, Wh	Discharge energy, Wh	Energy gain, %
5 mA till V=0.8 V	5 mA till V=0.6 V, or 4 s if V>0.6 V in 4 s	24 h 48 h 66 h	0.29	0.0356 0.0426 0.0468 ^a	0.0204 0.0204 0.0204	57.3 47.9 43.6

^a Cell continually charged at 0.1 V and could not reach 0.8 V.

Table 5. Control Validation cell: Flange closed, paste electrolyte [Ni/LiOH-LiBr-MgO/NiO]; Anode—Porous Ni C₆NC (14 cm², 2.66 g), submersed into electrolyte; Cathode—Pre-oxidized porous Ni C₆NC (3.8 × 3.8 cm), on top of electrolyte; Electrolyte—15 g LiOH + 75 g LiBr + 28 g MgO; Temperature 450 °C; Flow through Ar (Dry)

Charge I, T	Discharge I, T	Time	Charge energy, Wh	Discharge energy, Wh
	5 mA constant	0.75 h		0.0034
	discharge	5.37 h		0.0218 ^a

^a Cell was stopped at a voltage of 0.081 V.

Table 6. Thermodynamic parameters of the reaction of molybdenum metal with H₂O at 700 K [30].

Reaction	Mo + 2H ₂ O to MoO ₂ + 2H ₂			
	Mo	H ₂ O	MoO ₂	H ₂
Stoichiometry	1	2	1	2
HoF@700 K (kJ/mol)	10.451	-227.283	-560.881	11.723
S@700 K (J/molK)	50.604	219.368	102.685	155.545
H	10.451	-454.566	-560.881	23.446
G	-24.972	-761.681	-632.761	-194.317
ΔH _{rxn} (kJ/mol)=	-93.320			
ΔG _{rxn} (kJ/mol)=	-40.425			
T(K)=	700			
n=	4			
E°(700 K)=	0.105	Volts		

Table 7. Thermodynamic parameters of the reaction of nickel metal with O₂ at 700 K [30].

Reaction	Ni + (1/2)O ₂ to NiO		
	Ni	O ₂	NiO
Stoichiometry	1	0.5	1
HoF@700 K (kJ/mol)	12.351	12.552	-217.867
S@700 K (J/molK)	55.603	231.579	83.868
H	12.351	6.276	-217.867
G	-32.131	-86.356	-284.961
ΔH _{rxn} (kJ/mol)=	-242.770		
ΔG _{rxn} (kJ/mol)=	-166.474		
T(K)=	700		
n=	2		
E°(700 K)=	0.863	Volts	

Table 8. XRD of the electrolyte of the validation CIHT cell [Ni/LiOH-LiBr-MgO/NiO] after it produced 5.35 Wh at 1900% gain (Table 1). The mineral phases formed from the crystallized eutectic mixture were similar to those of melted and recrystallized starting material.

Identified Phases	Quantitative Analysis
LiBr	$13.7 \pm 0.1\%$ (584 Å)
$\text{Li}_5(\text{OH})_2\text{Br}_3$	$34.8 \pm 0.2\%$ (809 Å)
$\text{Li}_2\text{Br}(\text{OH})$	$20.9 \pm 0.2\%$ (430 Å)
MgO	$30.6 \pm 0.3\%$ (300 Å)

Table 9. The limiting oxygen reduction current at a nickel cathode determined in different molten alkaline electrolytes of KOH, NaOH, and LiOH with atmospheric air.

Molten Salt	Limiting O ₂ Reduction Current (mA/cm ²)
LiOH	1-2
NaOH	1-2
KOH	45-60

Table 10. The limiting oxygen reduction current at a nickel anode in different alkali hydroxide electrolytes maintained at 427 °C with different O₂ pressures measured by Antropov [15]^a.

Limiting O ₂ Reduction Current (mA/cm ²)		
p_{O_2}	NaOH	KOH
0.2 atm	0.66	69
1 atm	1.08	110

^a Subsequent rotating electrode studies by Hayashi [13] have shown that the oxygen reduction rate is first order in O₂ pressure at constant H₂O pressure sufficient to form OH⁻.

Table 11. The solid fuel reactants, maximum temperature of the run T , experimental net energy E_{net} , calculated theoretical maximum energy E_{mt} for conventional chemistry [30-32], and energy gain of hydrino catalyst systems.

Cell No.	Chemicals	T_{max} °C	E_{net} kJ	E_{mt} kJ	Energy Gain
115	6.0g NaOH + 25.0g Fe ₂ O ₃	565	8.7	-0.6	13.6
141	25.0g FeOOH	500.5	6.0	-1.4	4.3
147	6.0g NaOH (semicon grade) + 13.0g FeOOH	540	7.9	-1.4	5.6
166	6.0g NaOH (AD-1) + 25.0g FeOOH	530	10.8	-2.0	5.3
167	6.0g NaOH (semicon grade) + 25.0g FeOOH	571	10.7	-2.0	5.2
171	6.0g NaOH (AD-1) + 25.0g FeOOH (grinder mix)	617	9.3	-2.0	4.7
172	25.0g FeOOH (AD-1)	577	8.8	-1.4	6.3
181 ¹	25.0g FeOOH (AD-1)	563	7.4	-1.4	5.3
259	11.6g Mg(OH) ₂ + 21.6g FeCl ₃ + 100 psi H ₂ (0.0185 moles)	563	17.5	-3.6	4.9
314	4.8g LiOH + 32.3g CoI ₂ + 100 psi H ₂ (0.0185 moles)	603.4	9.9	-2.8	3.5
324 ²	5.8g Mg(OH) ₂ + 22.3g CuBr ₂ + 100 psi H ₂ (0.0185 moles)	564.5	11.9	-0.6	19.8
344	5.8g Mg(OH) ₂ + 30.8g MnI ₂ (Alfa) + 100 psi H ₂ (0.0185 moles)	614.2	11.4	13.2	inf
353	8.0g Mg(OH) ₂ + 37.3g SnI ₂ + 100 psi H ₂ (0.0185 moles)	546	6.9	13.6	inf
361	8.0g Mg(OH) ₂ + 21.9g CoBr ₂ + 100 psi H ₂ (0.0185 moles)	594	10.5	0.9	inf
371	12.2g Sr(OH) ₂ + 28.7g CuBr + 100 psi H ₂ (0.0185 moles)	617.6	14.5	-2.5	5.8
376 ³	12.2g Sr(OH) ₂ + 13.0g CoCl ₂ + 100 psi H ₂ (0.0185 moles)	662	42.6	-10.3	4.1
382	9.0g Mg(OH) ₂ + 19.5g YCl ₃ + 100 psi H ₂ (0.0185 moles)	577	8.8	-1.5	5.9
386	5.8g Mg(OH) ₂ + 22.3g CuBr ₂ + 100 psi H ₂ (0.0185 moles)	571	6.6	-0.6	11.0
446	9.8g Cu(OH) ₂ + 15.6g KHF ₂ + 104 psi H ₂ (0.0185 moles)	494	12.0	-2.2	5.5
460	8.8g Mg(OH) ₂ + 15.8g CrCl ₃ + 1 atm Ar	532	9.8	-2.2	4.5
465	9.8g Cu(OH) ₂ + 21.6g FeBr ₂ + 1 atm Ar	565	13.9	-1.6	8.7
466	9.8g Cu(OH) ₂ + 21.9g NiBr ₂ + 1 atm Ar	591	17.3	-0.9	19.2
467 ⁴	9.8g Cu(OH) ₂ + 21.9g CoBr ₂ + 1 atm Ar	576	12	-1.1	10.9
468	9.8g Cu(OH) ₂ + 13.0g NiCl ₂ + 1 atm Ar	552	8.7	0.6	inf
469	9.8g Cu(OH) ₂ + 21.5g MnBr ₂ + 1 atm Ar	602.7	14.2	9.8	inf
470 ⁵	9.8g Cu(OH) ₂ + 27.9g SnBr ₂ + 1atm Ar	598	16.4	-1.5	10.9
471 ⁶	9.8g Cu(OH) ₂ + 19.0g SnCl ₂ + 1 atm Ar	623	20.2	-1.2	16.8
475	9.8g Cu(OH) ₂ + 37.3.0g SnI ₂ + 1atm Ar	507	13.4	-4.1	3.3
479 ⁷	14.6g Cu(OH) ₂ + 15.0g InCl ₃ + 1atm Ar (repeat)	568	16.4	-0.6	27.3
490	9.3g Ni(OH) ₂ + 29.4g CaI ₂ + 1 atm Ar	588	6.8	-0.1	68.0
502 ⁸	11.1g Ca(OH) ₂ + 24.7g CeCl ₃ + 1atm Ar	564	10.2	-3.1	3.3
505 ⁹	13.9g Co(OH) ₂ + 37.9g CeBr ₃ + 1atm Ar	489	9.5	0.7	inf
506	13.9g Ni(OH) ₂ + 37.9g CeBr ₃ + 1atm Ar	517	11.2	0.5	inf
510	9.3g Co(OH) ₂ + 13.5g CuCl ₂ + 1atm Ar	554	7.8	-0.3	26.0
512 ¹⁰	9.3g Co(OH) ₂ + 23.3g CuBr ₂ + 1atm Ar	596	15	1.1	inf
513	9.3g Ni(OH) ₂ + 23.3g CuBr ₂ + 1atm Ar	626	17.3	0.9	inf
515	9.8gCu(OH) ₂ + 22.3g CuBr ₂ + 1 atm Ar	630	18.5	0	inf
530 ¹¹	9.3g Co(OH) ₂ + 23.3g CuBr ₂ + 1atm Ar	615	15.5	-0.2	77.5
531	9.3g Ni(OH) ₂ + 23.3g CuBr ₂ + 1atm Ar	599	13.9	-0.9	15.4
532 ¹²	9.8gCu(OH) ₂ + 23.3g CuBr ₂ + 1 atm Ar	672	21.6	-1.3	16.6
552 ¹³	9.8g Cu(OH) ₂ + 21.6g FeBr ₂ + 1atm Ar	580	13.1	-1.6	8.2
553	9.8g Cu(OH) ₂ + 21.9g NiBr ₂ + 1atm Ar	621	15.4	-0.9	17.1
582	9.3g Ni(OH) ₂ + 19.0g SnCl ₂ + 1 atm Ar	640	14.5	-3.7	3.9
594	20.0g Cu(OH) ₂ + 26.8g CuCl ₂ + 1 atm Ar (2x)	462	14.3	-2.6	5.5
611	1/2 of run 594 product (20.0g Cu(OH) ₂ + 26.8g CuCl ₂) + 0.9g H ₂ O	510	10.6	-0.3	35.3

¹ Thermal burst observed 150-170 °C

² Thermal burst observed 190-245 °C

³ Thermal burst observed 77-403 °C

⁴ Thermal burst observed 81-241°C

- ⁵ Thermal burst observed 71-152 °C
- ⁶ Thermal burst observed 54-174 °C
- ⁷ Thermal burst observed 87-169 °C
- ⁸ Thermal burst observed 73-187 °C
- ⁹ Thermal burst observed 98-154 °C
- ¹⁰ Thermal burst observed 85-201 °C
- ¹¹ Thermal burst observed 78-189 °C
- ¹² Thermal burst observed 360-520 °C
- ¹³ Thermal burst observed 79-187 °C

Table 12. ESI-ToFMS results obtained on the same sample analyzed by ToF-SIMS (Figures 11A-C) comprising K₂CO₃-KCl (30:70 wt%) getter from the scale-up 5 W stack of 10 CIHT cells comprising [Mo/LiOH-LiBr-MgO/NiO] that output 1029 Wh at 137% gain having the upfield shifted MAS NMR spectral peaks. Multimer clusters of matrix compounds with dihydrogen as part of the structure, M:H₂ (M = KCl, KOH, or K₂CO₃) consistent with H₂(1/p) as a complex in the structure were observed. These clusters were not observed in controls comprising the matrix exposed to H₂.

Hydrino Compound or Fragment	Nominal Mass m/e	Observed m/e	Calculated m/e	Difference Between Observed and Calculated m/e
K ⁺ (KCl:H ₂)	115	114.9118	114.9114	0.0004
K ⁺ KHKOH:H ₂ or K ⁺ K ₂ O:(H ₂) ₂	137	136.9583	136.9173	0.0410
K ⁺ [(KCl) ₃ :H ₂]	263	262.7772	262.7770	0.0002
K ⁺ [H ₂ O(K ₂ CO ₃) ₂ :(H ₂)]	335	334.7661	334.8137	0.0476
K ⁺ [H ₂ O(K ₂ CO ₃) ₂ :(H ₂) ₂]	337	336.7324	336.8293	0.0969
K ⁺ [H ₂ O(K ₂ CO ₃) ₂ :(H ₂) ₃]	339	338.7099	338.8450	0.1351

Figure 1. CIHT cell schematic in the discharge mode.

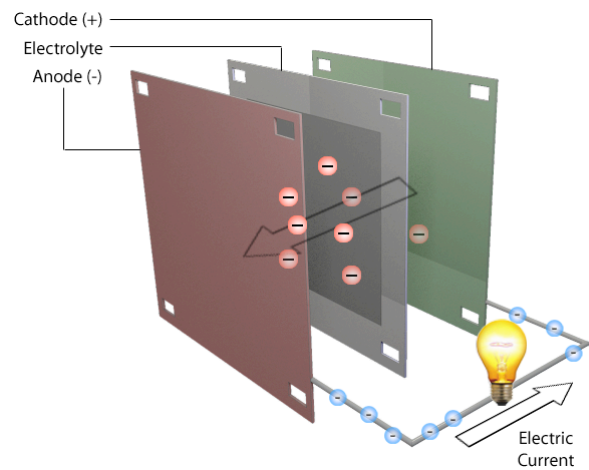


Figure 2. The charge and discharge voltage and current over time of the validation CIHT cell [Ni/LiOH-LiBr-MgO/NiO] of Table 1 recorded on day 37 with the digital oscilloscope.

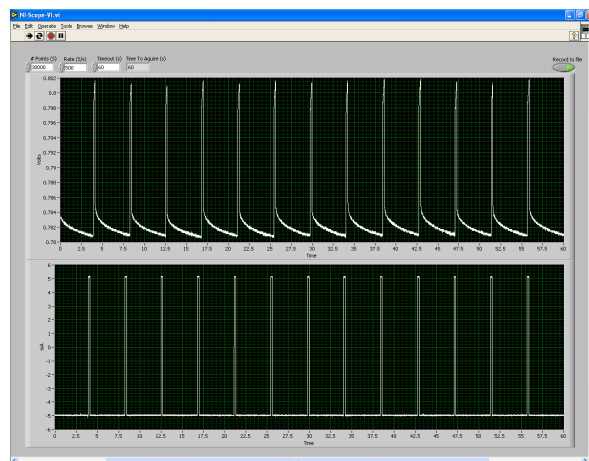


Figure 3. The accumulated charge and discharge energies and the corresponding electrical energy gain over time of the validation CIHT cell [Ni/LiOH-LiBr-MgO/NiO] of Table 1.

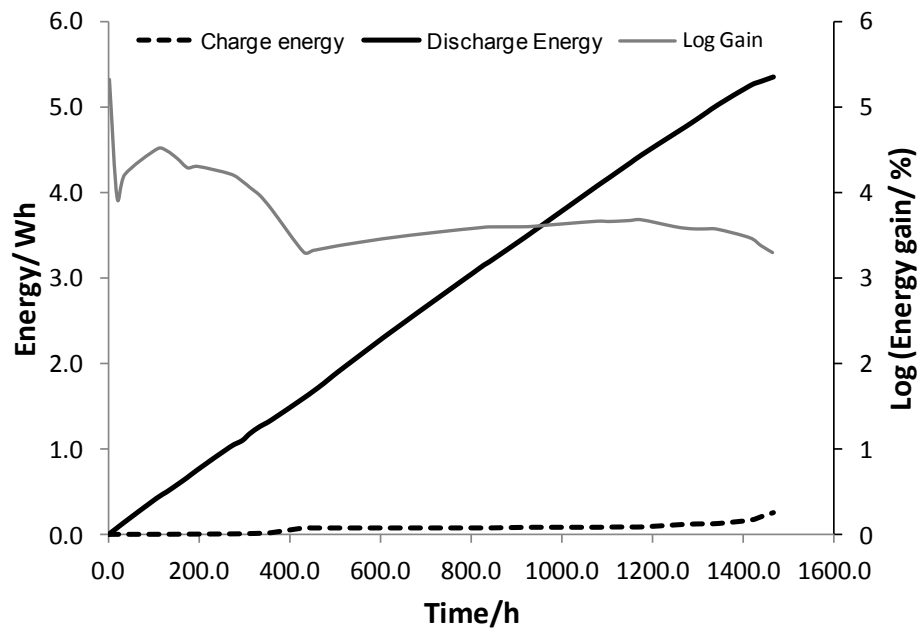


Figure 4. SEM (top) and EDS (bottom) results of validation CIHT cell [Ni/LiOH-LiBr-MgO/NiO] of Table 1 showing residual MgO with no corrosion of the Ni mesh sample cut from the anode after two months of continuous operation.

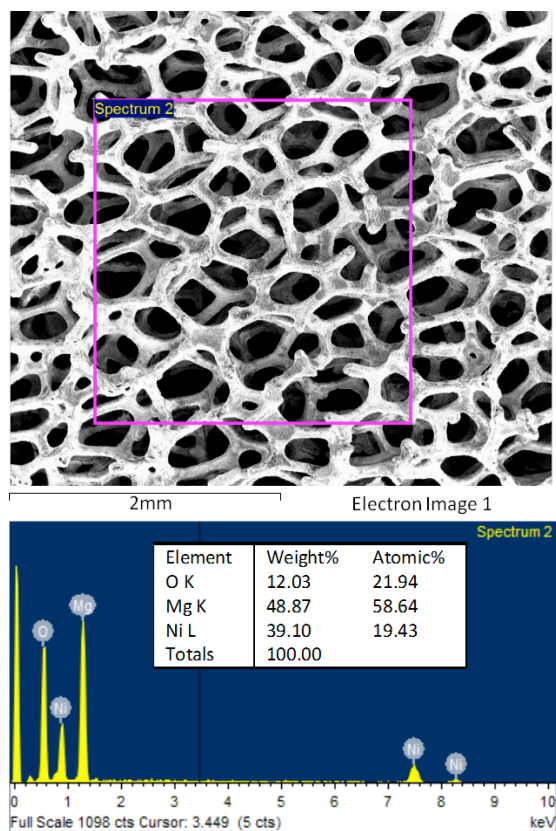
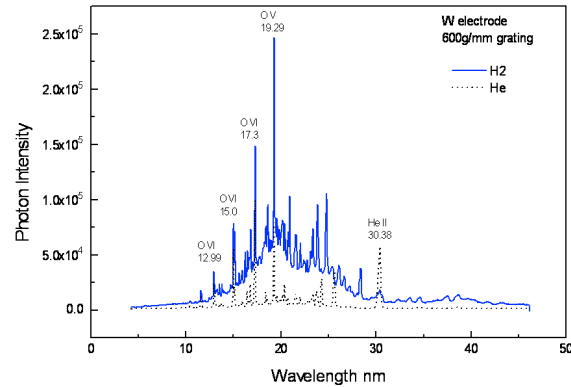


Figure 5. Emission spectra (3-46 nm) of electron-beam-initiated, high-voltage pulsed discharges in hydrogen (solid) and helium (dashed) with W electrodes recorded by the EUV grazing incidence spectrometer using the 600 lines/mm grating and 1000 superpositions showing continuum radiation in the 10 to 30 nm that was observed for hydrogen only.



Figures 6A-B. The temporal evolution of Balmer α line profile width recorded on hydrogen plasmas at 100 mTorr and an RF coupled power of 200 Watt over a three-hour plasma duration. (A) Initial populations showing only warm and cold hydrogen. (B) The emission profile showing the fast H population after 3 hours of maintaining the hydrogen plasma without flow. A fast population of H atoms with energies greater than 100 eV was observed later in time; whereas, only mildly warm H atoms with energies of 7 eV were observed in the beginning of the experiment.

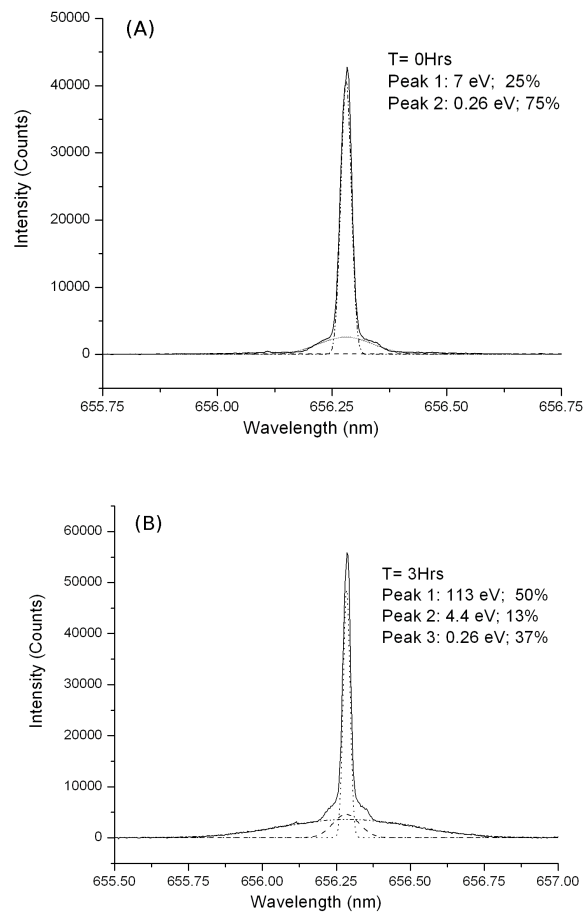


Figure 7. Dark matter ring in galaxy cluster. This Hubble Space Telescope composite image shows a ghostly “ring” of dark matter in the galaxy cluster Cl 0024+17. The ring is one of the strongest pieces of evidence to date for the existence of dark matter, a prior unknown substance that pervades the universe. Courtesy of NASA, M.J. Jee and H. Ford (Johns Hopkins University).

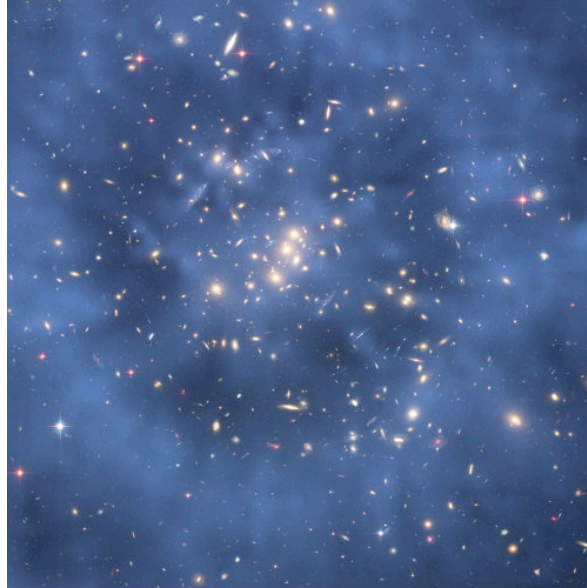


Figure 8. ^1H MAS NMR spectrum relative to external TMS of the initial KOH-KCl (1:1) getter that shows the known down-field shifted matrix peak at +4.41 ppm.

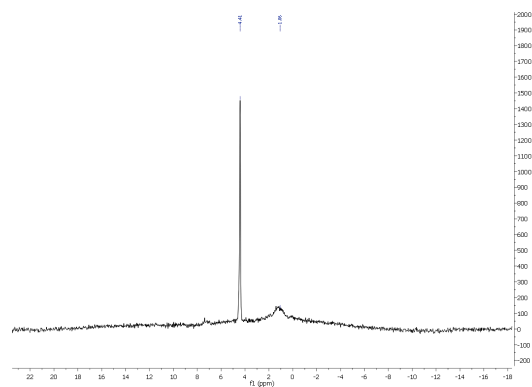


Figure 9. ^1H MAS NMR spectrum relative to external TMS of the KOH-KCl (1:1) getter from the scale-up 5 W stack of 10 CIHT cells comprising [Mo/LiOH-LiBr-MgO/NiO] that output 1029 Wh at 137% gain that shows upfield shifted matrix peaks at -4.06 and -4.41 ppm. The small symmetrically spaced peaks are spinning side bands.

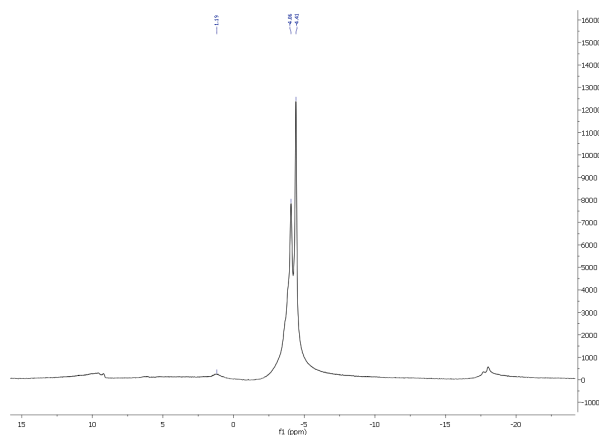
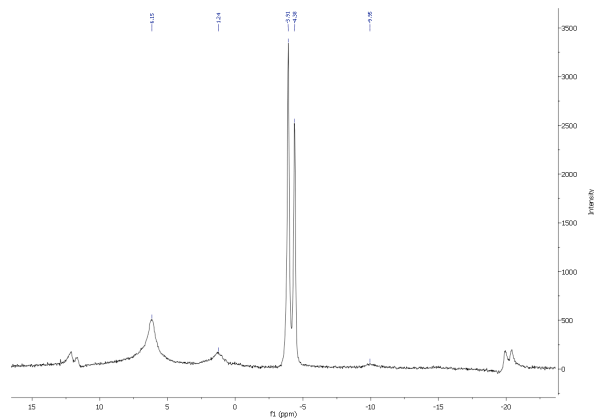
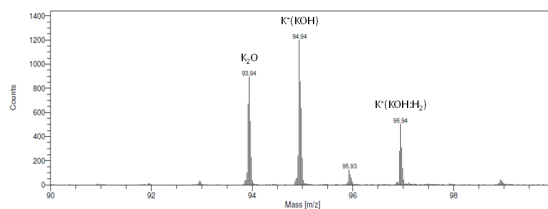


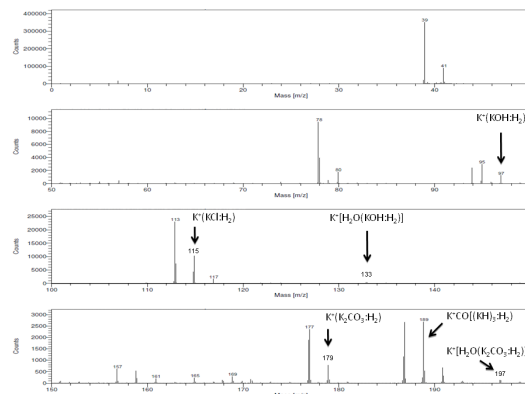
Figure 10. ^1H MAS NMR spectrum relative to external TMS of the K + KCl getter from the solid fuel reaction of FeOOH that shows upfield shifted matrix peaks at -3.91 and -4.38 ppm. The small symmetrically spaced peaks are spinning side bands.



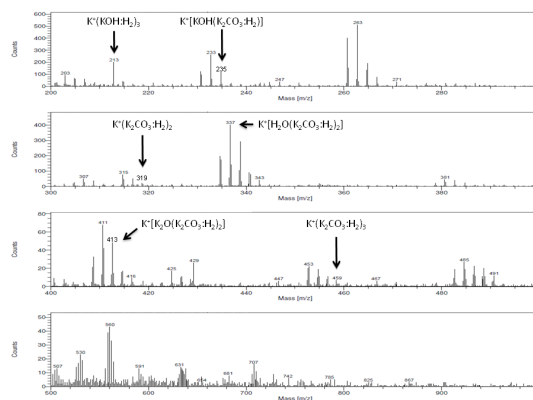
Figures 11A-C. ToF-SIMS spectrum of $\text{K}_2\text{CO}_3\text{-KCl}$ (30:70 wt%) getter from the scale-up 5 W stack of 10 CIHT cells comprising $[\text{Mo/LiOH-LiBr-MgO/NiO}]$ that output 1029 Wh at 137% gain having the upfield shifted MAS NMR spectral peaks. Multimer clusters of matrix compounds with di-hydrogen as part of the structure, M:H_2 ($\text{M} = \text{KOH}$ or K_2CO_3) such as $\text{K}^+(\text{KOH:H}_2)_n$ and $\text{K}^+(\text{K}_2\text{CO}_3\text{:H}_2)_n$ consistent with $\text{H}_2(1/p)$ as a complex in the structure were observed. These clusters were not observed in controls comprising the matrix exposed to H_2 . (A) Positive ToF-SIMS, $m/e = 90$ to 100 region. (B) Positive ToF-SIMS, $m/e = 0$ to 200 region. (C) Positive ToF-SIMS, $m/e = 200$ to 1000 region.



(A)

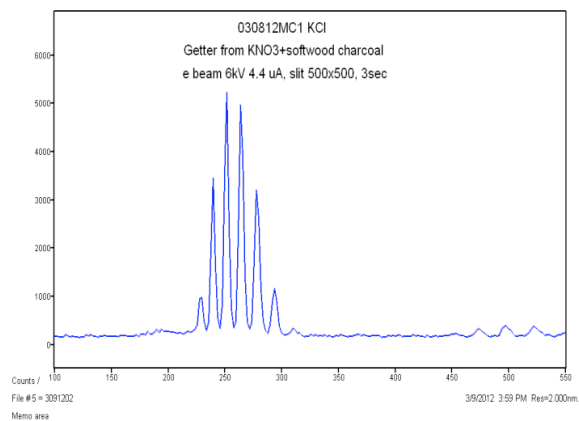


(B)

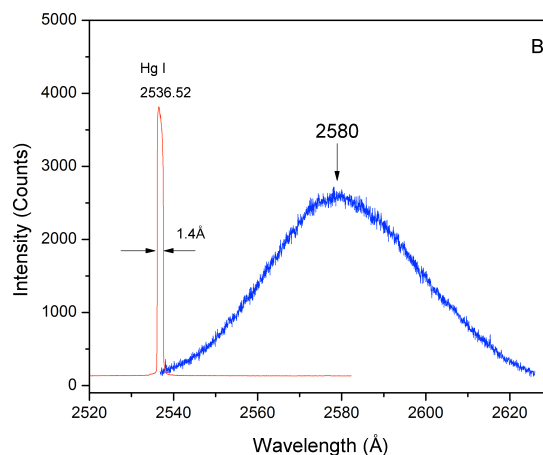
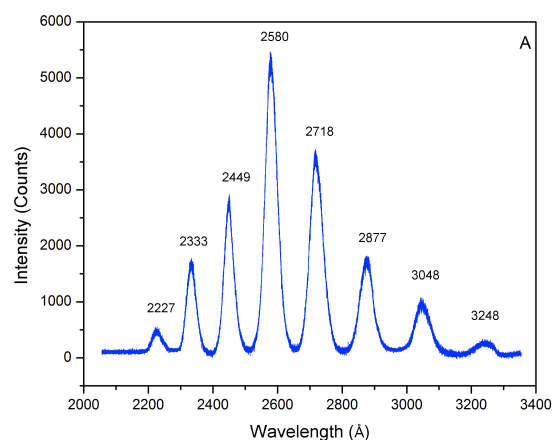


(C)

Figure 12. The electron-beam excitation emission spectrum recorded on the KCl getter from a sealed reactor of the gun powder reaction, KNO_3 with softwood charcoal having the formulation $\text{C}_7\text{H}_4\text{O}$, showing the 260 nm band comprising the peaks Q(0), R(0), R(1), R(2), P(1), P(2), P(3), and P(4) of $\text{H}_2(1/4)$.



Figures 13A-C. The high resolution visible spectrum of the 260 nm band of the KCl getter of the gun powder reaction, KNO_3 with softwood charcoal having the formulation $\text{C}_7\text{H}_4\text{O}$. No structure was observed eliminating ro-vibrational bands of a common molecule as the source and supporting the assignment as broad rotational emission of $\text{H}_2(1/4)$ within the $v=1 \rightarrow v=0$ transition. (A) Q(0), R(0), R(1), R(2), P(1), P(2), P(3), and P(4) recorded with an e-beam energy of 6 keV, a current of 10 μA , an accumulation time of 300 s, and a slit width 1000 μm corresponding to a resolution of 3.0 \AA . (B) Q(0) peak at 2580 \AA and Hg I 2536.52 \AA peak recorded with an e-beam energy of 6 keV, a current of 15 μA , an accumulation time of 300 s, and a slit width of 500 μm corresponding to a resolution of 1.4 \AA . (C) Q(0) peak at 2580 \AA and Hg I 2536.52 \AA peak recorded with an e-beam energy of 6 keV, a current of 23 μA , an accumulation time of 2500 s, and a slit width of 100 μm corresponding to a resolution of 0.25 \AA and a wavelength accuracy of $\pm 1.0 \text{ \AA}$ verified with the 2536.52 \AA and other Hg I lines.



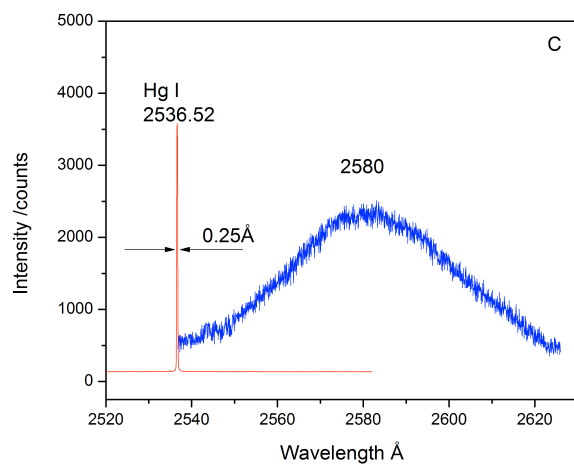


Figure 14. The Raman spectrum obtained on the KCl + K getter in the sealed FeOOH + H₂ + Ni screen dissociator solid fuels reactor using the Thermo Scientific DXR SmartRaman spectrometer and the 532 nm laser showing the peak corresponding to P(1) of the series at 2594 cm⁻¹. The sharp peak at 1950 cm⁻¹ matches the free rotor energy of H₂(1/4) (0.2414 eV) to four significant figures. The peak at 2342 cm⁻¹ is N₂.

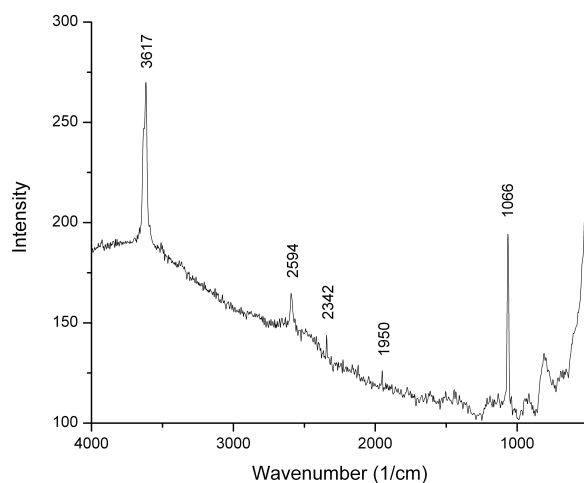


Figure 15. The corresponding FTIR spectrum of Figure 14 obtained on the KCl + K getter of the FeOOH solid fuel also showing the new sharp peak at 1950 cm^{-1} that matches the free rotor energy of $\text{H}_2(1/4)$.

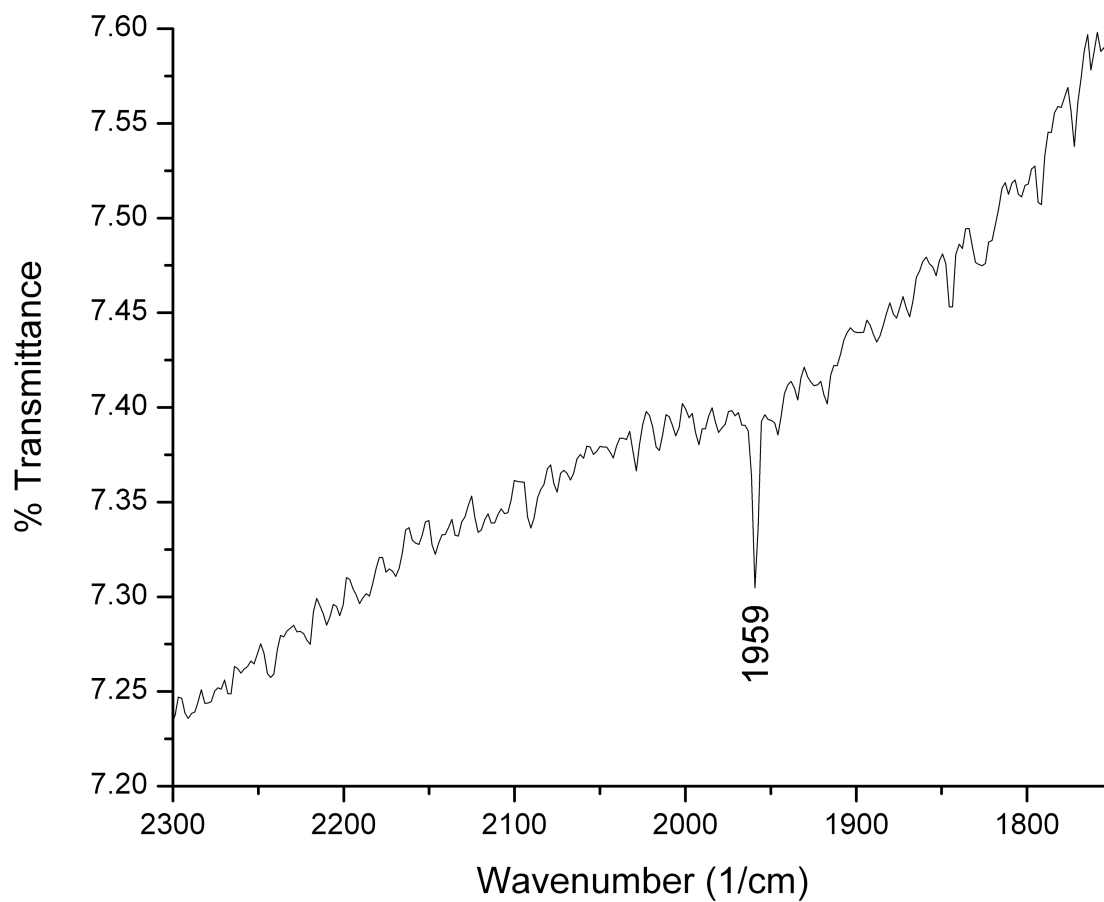


Figure 16. The XPS spectrum of the Ni cathode in a K_2CO_3 electrolysis cell having a peak at 496.4 eV assigned to $\text{H}_2(1/4)$ wherein the Na KLL Auger peak at 493 eV was eliminated due to the complete absence of the typically more intense Na 1s (1072 eV) as well as the Na $2p_{1/2}$ (31 eV) and Na 2s (64 eV).

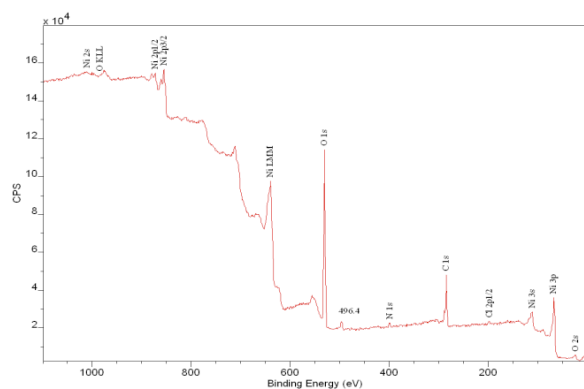


Figure 17. Spectrum of the KOH getter from the 65 mW, eight-layer CIHT stack, each cell comprising [Mo/LiBr-LiOH-MgO/NiO], that showed intense (6000 count) e-beam excitation emission of the 260 nm band profile recorded in Raman mode using the Aramis with a HeCd 325 nm laser in microscope mode with a magnification of 40X. An intense series of 1000 cm^{-1} equal-energy spaced Raman peaks were observed at 8340, 9438, 10467, 11478, 12457, 13433, and 14402 cm^{-1} with the maximum peak intensity at 12,457 cm^{-1} .

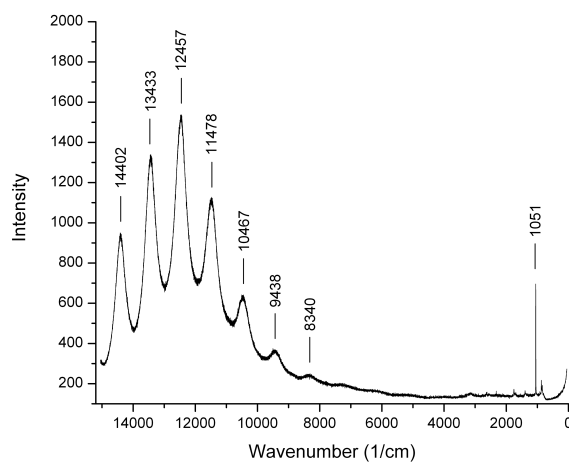


Figure 18. The deconvolution of the photoluminescence spectrum converted from the Raman spectrum shown in Figure 30 reveals that the Raman spectrum is the superposition of the second order fluorescence of the 260 nm band first observed by e-beam excitation and a separate continuum emission band having its maximum intensity at green wavelengths. The black line is the raw data, and the dotted line is the sum of the two deconvolved components.

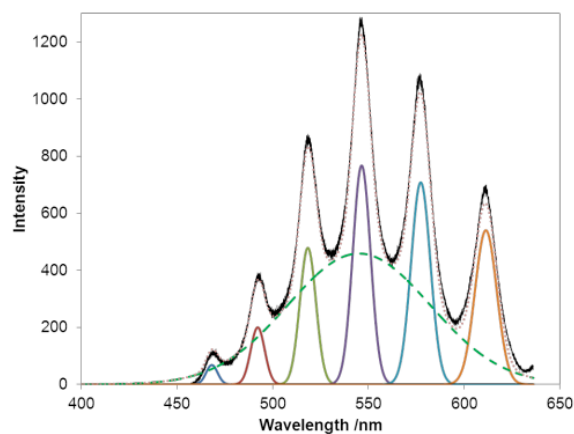


Figure 19. The superposition of the spectrum of the 260 nm band of the KCl getter of the gun powder reaction and that corresponding to the first order fluorescence or photoluminescence spectrum calculated from the peak positions of Figure 30 wherein the raw data energy spacing of 1000 cm^{-1} or 0.1234 eV matches the second order rotational spectrum of $\text{H}_2(1/4)$ very well. Other than the effect of the KOH versus KCl matrices, the spectra match. Considering maximum peak intensity at $12,457\text{ cm}^{-1}$ in Figure 30 being Q(0), the assignments are Q(0), R(0), R(1), R(2), R(3), P(1), and P(2) at $12,457$, $11,478$, $10,467$, 9438 , 8340 , $13,433$, and $14,402\text{ cm}^{-1}$.

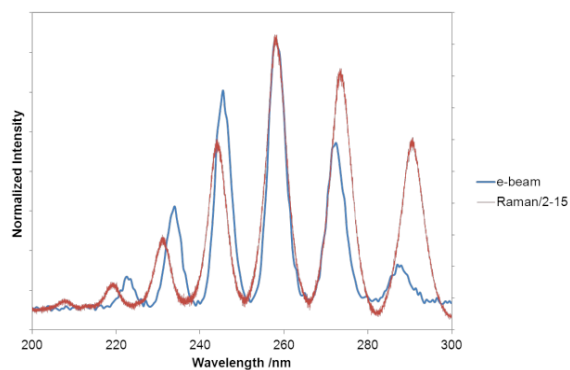


Figure 20. Raman-mode spectrum of K_2CO_3 -KCl (1:1) getter of the cell [laminated-CNi₆ 1.5"×1.5" + CNi₈ 1.5"×1.5" + Mo 1"×1" CNi₈ + 1.5"×1.5" + Ag 1"×1" + CNi₈ 1.5"×1.5"+ CNi₆ 1.5"×1.5")/LiOH-LiBr-MgO/NiO] (50 mA charge and discharge current; 2.65 Wh discharge energy, 200% gain) wherein the 260 nm e-beam band was observed intensely. The laser-excited second-order fluorescence band having a slight shift due to the different matrix was also observed to extend to 17,000 cm^{-1} with higher orders beyond that to the maximum scanned range to 22,000 cm^{-1} . The series comprised Q(0), R(0), R(1), R(2), R(3), P(1), P(2), P(3), P(4), and P(5) at 12,199, 11,207, 10,191, 9141, 8100, 13,183, 14,168, 15,121, 16,064, and 16,993 cm^{-1} , respectively. The 15,925 cm^{-1} doublet is the second order of the doublet at 1096 and 1068 cm^{-1} , and the peak at 15,391 cm^{-1} is the 325 nm laser second order line.

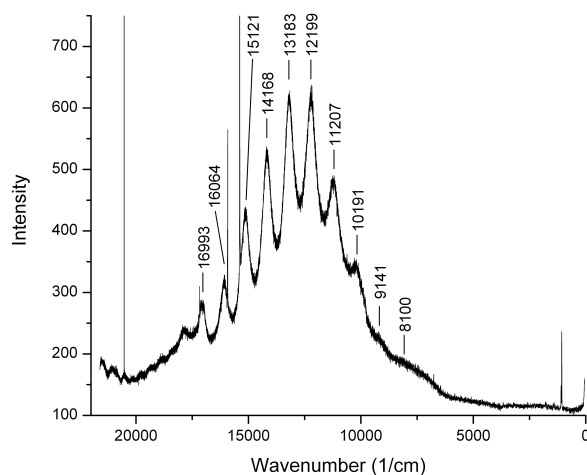


Figure 21. Raman-mode spectrum of the KOH-KCl (1:1) getter from the scale-up 5 W stack of 10 CIHT cells comprising [Mo/LiOH-LiBr-MgO/NiO] that output 1029 Wh at 137% gain that shows up-field shifted matrix peaks at -4.06 and -4.41 ppm (Figure 9). The laser-excited second-order fluorescence band was also observed to extend to $17,000\text{ cm}^{-1}$ with higher orders beyond that to the maximum scanned range to $22,000\text{ cm}^{-1}$. Q(0), R(0), R(1), R(2), R(3), R(4), P(1), P(2), P(3), P(4), P(5), and P(6) were observed at 12,199, 11,207, 10,191, 9141, 8100, 13,183, 14,168, 15,121, 16,064, 16,993, and $17,892\text{ cm}^{-1}$, respectively.

